

Session 1P1

Poster Session 2

Mobile Wireless Communication System Antennas for 260 MHz-band	274
<i>H. Kawakami (Antenna Giken Corp., Japan);</i>	
Compact Surface-mount UWB Monopole Antenna for Mobile Applications	276
<i>C. Y. Wu (Industrial Technology Research Institute, Taiwan); C. L. Tango (Industrial Technology Research Institute, Taiwan); A. C. Chenn (Industrial Technology Research Institute, Taiwan);</i>	
TEC Measurements through GPS and Artificial Intelligence	279
<i>V. Barrile (Univ. Mediterranea, Italy); M. Cacciola (Univ. Mediterranea, Italy); F. Cotroneo (Univ. Mediterranea, Italy); F. C. Morabito (Univ. Mediterranea, Italy); M. Versaci (Univ. Mediterranea, Italy);</i>	
Reliability and Availability of GPS Measures in Airport Landing Systems	280
<i>V. Barrile (University "Mediterranea of Reggio Calabria, Italy); M. Cacciola (University "Mediterranea of Reggio Calabria, Italy); F. Cotroneo (University "Mediterranea of Reggio Calabria, Italy);</i>	
Electromagnetic Scattering by Rough Surfaces with Spatially Varying Impedance	284
<i>M. Spivack (University of Cambridge, UK); N. S. Basra (University of Cambridge, UK);</i>	
Development of the Pulsed Direct Current Iontophoresis and Its Clinical Application	285
<i>M. Akimoto (Kanto Gakuin University, Japan); M. Kawahara (I.C.I. Cosmetics Japan, Japan); M. Matsumoto (I.C.I. Cosmetics Japan, Japan); H. Matsubayashi (I.C.I. Cosmetics Japan, Japan);</i>	
Design of Reduced-size Branch-line Couplers with Series Capacitors	291
<i>T. Kawai (University of Hyogo, Japan); Y. Kokubo (University of Hyogo, Japan); I. Ohta (University of Hyogo, Japan);</i>	
Plane Wave Scattering by an Array of Pseudochiral Cylinders	292
<i>M. Polewski (Gdansk University of Technology, Poland); R. Lech (Gdansk University of Technology, Poland); J. Mazur (Gdansk University of Technology, Poland);</i>	
Electromagnetic Field for Randomly Oriented Particle Located in Laser Beam	293
<i>Y. P. Han (Xidian University, China); H. Y. Zhang (Xidian University, China);</i>	
Corrector Packaging for Heating inside a Domestic Microwave Oven	294
<i>A. Rhattoy (UniversitéMoulay Ismail Meknes, Morocco); S. Bri (UniversitéMoulay Ismail Meknes, Morocco); M. Audhuy-Peudeceder (ENSEEIH-INT, France);</i>	
A WEB Application for Electromagnetic Structures	295
<i>A. S. B. Lopes (CEFETRN/NUTEL, Brazil); F. M. Sales Junior (CEFETRN/NUTEL, Brazil); J. R. S. Oliveira (CEFETRN/NUTEL, Brazil);</i>	
Computation of Resonant Frequencies of Any Shaped Dielectric Resonators by CFDTD	296
<i>A. Shahvarpour (K.N.Toosi University of Technology, Iran); M. S. Abrishamian (K.N.Toosi University of Technology, Iran);</i>	
A Novel Transmission Line Model for Analyzing Bowtie Patch Antennas	301
<i>K. Moussakhani (Amirkabir University of Technology, Iran); A. Ghorbani (Amirkabir University of Technology, Iran);</i>	

Mobile Wireless Communication System Antennas for 260 MHz-band

H. Kawakami

Antenna Giken Corp., Japan

1. Introduction

Automotive mounted antennae are often vertically orientated $1/4$ wave antennae because the body of the car can be used as an effective reflective infinite ground plane. This ground plane permits the radiation pattern of a mounted $1/4$ wave antenna to behave like that of a $1/2$ wave antenna. The $1/4$ wave antenna has a low cost and is also compact in size. This compact quality is important in automobile mounted antennae because it reduces the risk of antenna damage and also does not create difficulty when restrictions on the height of a car's profile are present. This paper presents a design of an antenna that is compact like a $1/4$ wave antenna but can behave as closely as possible to a $1/2$ wave antenna without the presence of an effective infinite ground plane.

The $1/4$ helical antenna is well known, but this paper presents the design of a helical antenna that meets our height design requirements. Specifically, a monopole antenna with a height of under 300 mm is desired. The standing wave ratio must be under 2.0 in the frequency band of interest. The height of the helical element must remain at some constant so the pitch and diameter of the spiral were optimized. An improvement in gain was obtained by using a small finite reflection plate.

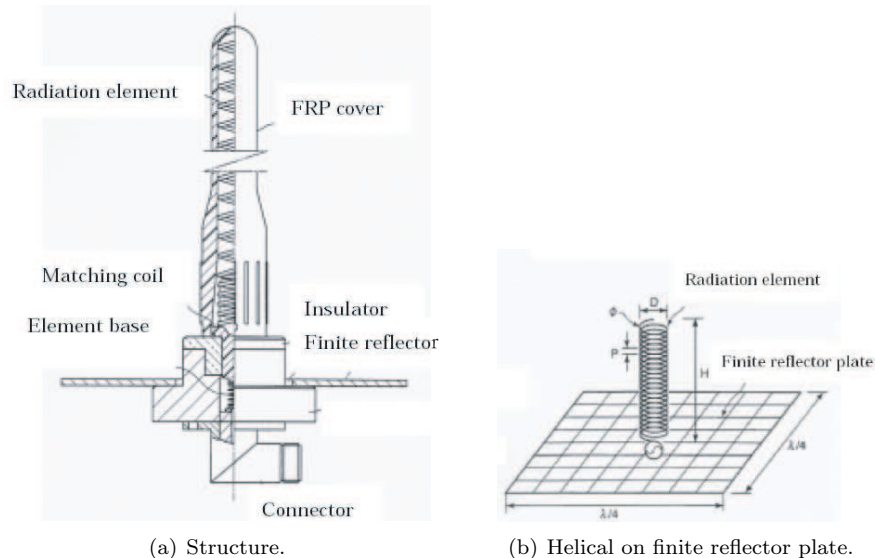


Figure 1: Mobile wireless communication system antennas for 260 MHz-Band.

2. Antenna Structure

As mentioned earlier, $1/4$ wave antennae are usually used in mobile radio devices when a large ground plane is available. The efficiency of an antenna depends on the loss due to the mismatch between the impedance of the receiving antenna and the transmitter. The impedance of any portable receiving antenna can be quite variable depending on how it is mounted: for example, carried by a human or affixed to a car. Also of concern is the unpredictability of the height of the antenna above a ground plane. This creates an unstable state because of the high frequency current flowing within the standard antenna. Our antenna has been designed to deal with this instability and is more efficient than a standard $1/4$ wavelength antenna.

Figure 1(a) shows the basic structure of our helical antenna as detailed in [1]. The figure shows a finite reflected plate. Figure 1(b) is the simplified model of the antenna with a helical antenna above a finite reflector plate. The center frequency was chosen to be 265 MHz. With the height H of the helical element fixed to be 220 mm, we adjust pitch P and diameter D of the spiral. Shown in Figure 2 is a 2D plot of the horizontal gain as a function of P and D . There is a region where 2 dBi gain is realizable.

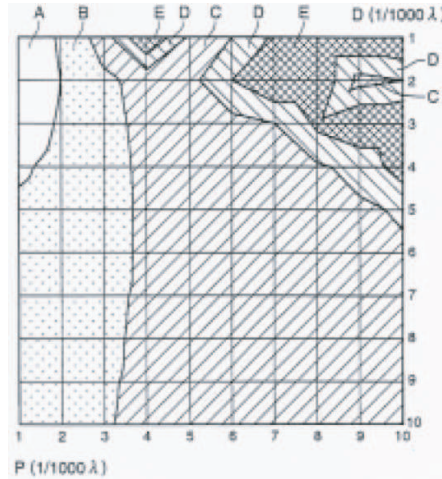


Figure 2: Horizontal gain of mapping for helical antenna.

A: 2 dBi more than B: 1.5 dBi C: 1.5 dBi D: 0.5 dBi E: 0.5 dBi

3. Experimental Result

The antenna can be adjusted to a particular resonant frequency to create the VSWR pattern shown in Figure (3). A good impedance match is found between 262 to 275 MHz where the VSWR is lower than 2.0 which corresponds to -9.5 dB. The vertical radiation pattern of this antenna is compared with the pattern from a $1/2$ wavelength antenna in Figure (4). The actual gain was about -1 to -2 dB but the horizontal radiation pattern is omni directional.

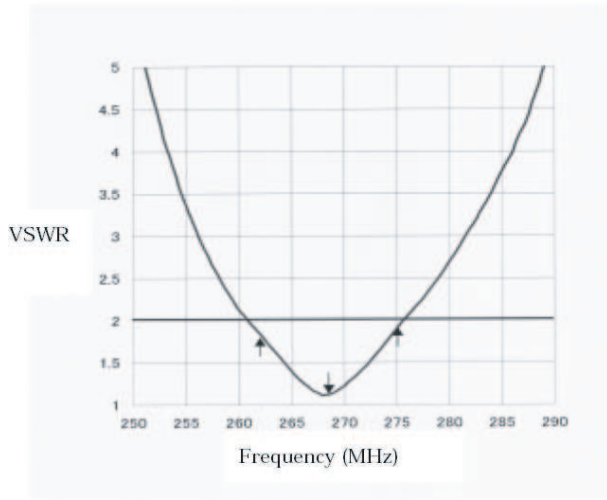


Figure 3: Characteristic of VSWR.

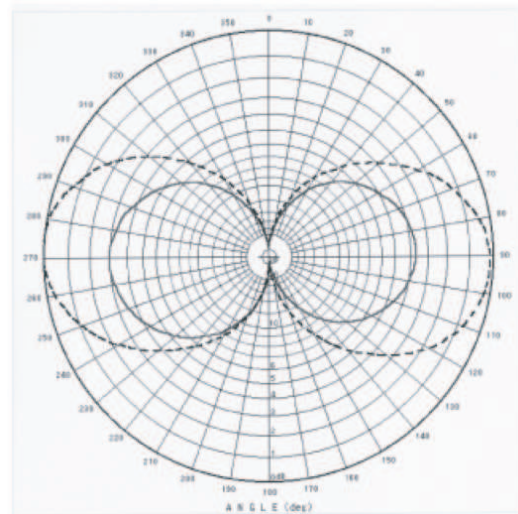


Figure 4: Vertical Radiation Pattern. (Dotted line: $1/2$ wavelength, Solid line: this antenna)

4. Conclusion

The effectiveness of a finite reflector plate with a helical antenna is examined. There is an increase of gain in the horizontal direction and a reduction in antenna size. This type of antenna is more immune to the effects of the surrounding environment. This antenna is very practical and may be used when it is necessary to mount antennae on cars with plastic outer bodies such as ambulances. Changes in the shape of the radiating element and simplification of the feed line will be the future work on this project.

REFERENCES

1. Kawakami, et. al, *Patent No. 3093712*.

Compact Surface-mount UWB Monopole Antenna for Mobile Applications

C. Y. Wu, C. L. Tang, and A. C. Chen
Industrial Technology Research Institute, Taiwan

Abstract—In this paper, a novel surface-mount ultra-wideband (UWB) monopole antenna with a compact size of only $12.5 \times 9 \times 1.5 \text{ mm}^3$ is obtained by folding a metal-plate onto a low-profile rectangular-box foam base. By carefully adding a matching slit on the upper side of metal-plate, the antenna can achieve good impedance matching over a very wide bandwidth of about 7.97 GHz (3.03–11.0 GHz, defined by 2:1 VSWR). Experimental results of a constructed prototype of the proposed antenna are presented.

1. Introduction

In the recent years, short range and high data rate wireless communication is applied in multimedia device. UWB radio technology can meet these requests. Planar antennas have many advantages, such as low profile, small size and easy to fabricate, which are suitable for portable devices. There are several UWB planar antenna designs, including planar metal-plate antenna [1], half-disk antenna [2], and planar horn antenna [3], which have been reported.

In this paper, a novel surface-mount UWB monopole antenna, which is suitable for metal stamping processing and low fabricating cost, is presented. The proposed antenna has a compact structure, which makes it easy to fit in any possible margin within the housing of a mobile/hand-held wireless device, thus leading to an internal UWB antenna.

2. Antenna Design

Figure 1 shows the proposed UWB monopole antenna mounted at the front surface of a 0.8 mm thick FR4 substrate ($\epsilon_r = 4.4$). The ground plane (length 40 mm and width 60 mm) printed on the back surface of the FR4 substrate can be considered as the system circuit board of a wireless access point. The proposed UWB antenna is easily constructed by folding a metal plate into a rectangular form base of compact size $12.5 \times 9 \times 1.5 \text{ mm}^3$.

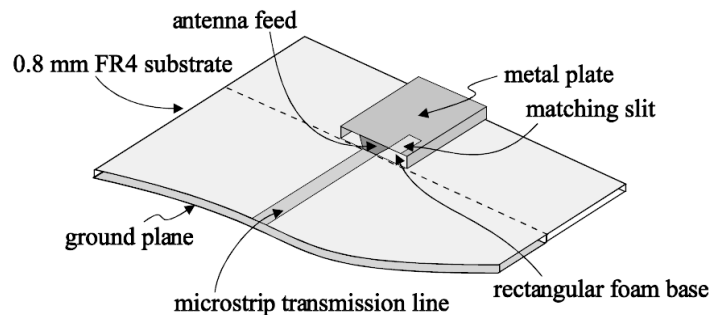


Figure 1: Proposed surface-mounted monopole antenna mounted on the PCB board of a wireless access point.

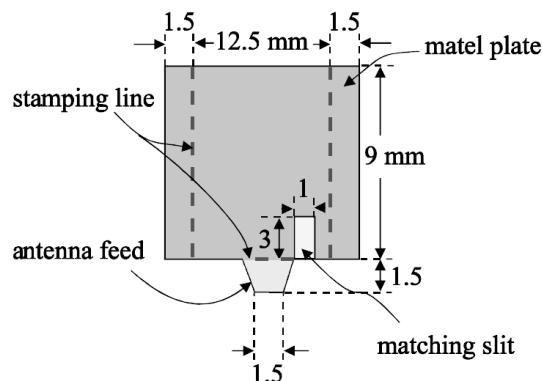


Figure 2: Planar structure of the unfolded metal plate (dashed lines on the metal plate are the stamping line).

Figure 2 shows the detailed dimension of the metal plate. The size of the metal plate is $15.5 \times 9 \text{ mm}^2$ with a matching slit of $1 \times 3 \text{ mm}$ near the antenna feed. The lowest resonant frequency and the highest resonant frequency of proposed antenna were mainly controlled by length and width of the metal-plate. Broadband matching technique is the key point in UWB antenna design, by carefully adding a matching slit on the upper side of metal-plate, the antenna can achieve a good impedance matching over a very wide bandwidth. With the matching slit, the current distribution on the surface of the radiation conductor can be altered. By carefully tuning the width and length of the matching slit, a very wide band impedance matching (defined by 2:1 VSWR) from 3.03 GHz to 11.0 GHz is obtained. This result is mainly due to the asymmetrically antenna structure which will lead to asymmetrically current path and it is helpful to achieve broadband impedance matching. Thus, the mechanism of the matching slit is similar to asymmetrically feed mentioned in [4].

The radiation energy of the proposed antenna is activated by the antenna feed via the microstrip transmission line. To accomplish the impedance matching between the metal plate and the microstrip transmission line, there are trapezoid-shaped metallic strip formed between the metal plate and the microstrip transmission line.

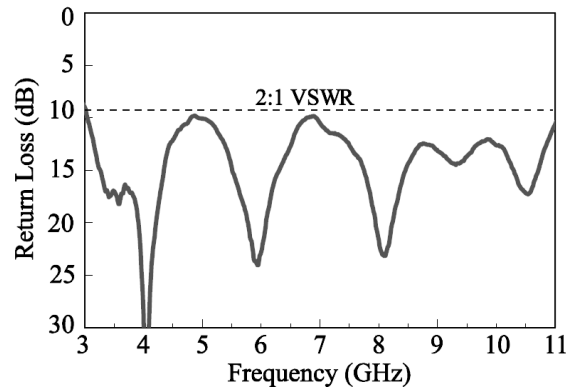


Figure 3: Measured return loss of the proposed antenna.

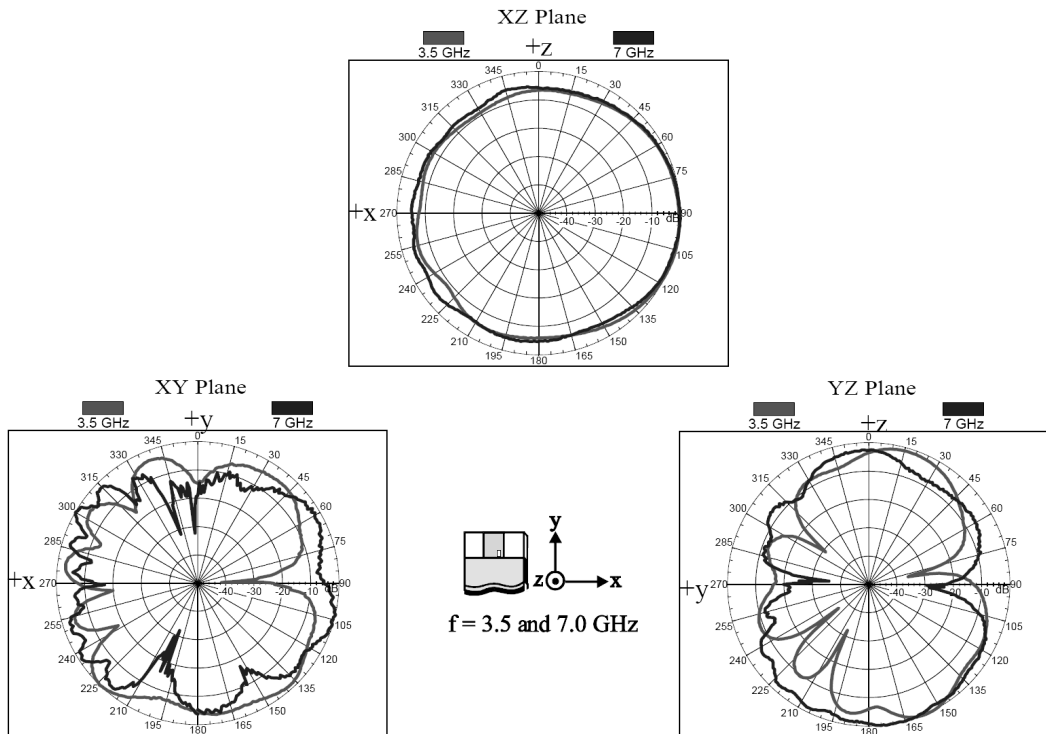


Figure 4: Measured radiation patterns at 3.5 and 7.0 GHz.

3. Experimental Results

Figure 2 shows the measured return loss for the proposed antenna. From the results, it clearly indicates that the impedance bandwidth, defined by 2:1 VSWR, is as large as 7.97 GHz. Thus, the proposed antenna can cover the full band of DS-UWB [5].

The far-field radiation characteristic across UWB bandwidth of the proposed antenna is also studied. The far-field radiation pattern (only co-polarization is showed) of the proposed antenna at 3.5 GHz (light color line) and 7.0 GHz (deep color line) are shown as Figure 4. It is first observed that, in vertical cut of azimuthal plane (or x - z plane), the radiation pattern of antenna shows an omni-directional radiation characteristic, but apparently shift to the $-x$ direction. It is mainly due to the ground plane effect. In the radiation pattern of horizontal cut of y - z plane, especially at 7.0 GHz, it is also seen that there are two null in $\pm y$ direction. According to what has been mentioned above, in brief, it is a monopole-like radiation pattern. The measured antenna gain against frequency is presented in Figure 5. Across the impedance bandwidth in 3.0 to 10.0 GHz, the measured antenna gain increases from about 1.7 to 3.3 dBi with increasing frequencies. Measured peak antenna in the lower band and the higher band of DS-UWB is about 2.4 dBi and 3.2 dBi, respectively.

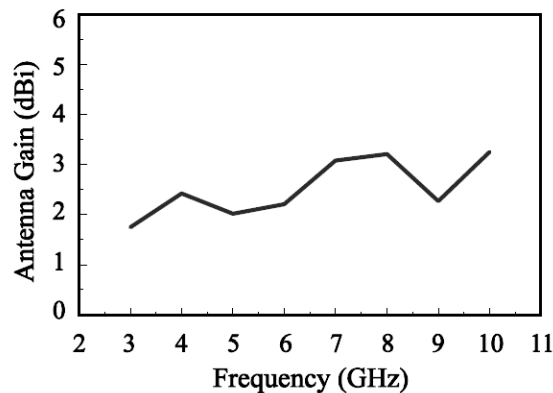


Figure 5: Measure peak antenna gain against frequency of the proposed antenna.

4. Conclusions

A compact surface-mount UWB chip antenna, which mainly constructed by stamping the metal plate has been fabricated and studied. Results indicate that the constructed prototype showed a very wide-impedance bandwidths covering the lower and higher bands of DS-UWB. Good antenna gain in the operation bands is also obtained. In addition, the antenna has a compact structure, which makes it easy to fit in any possible margin within the housing of a mobile/hand-held wireless device, thus leading to an internal UWB antenna. The small size UWB antenna is also suitable for surface-mountable fabrication process. Thus it can effectively reduce the overall manufacturing cost.

REFERENCES

1. Wong, K. L., T. C. Tseng, and P. L. Teng, "Low-profile ultra-wideband antenna for mobile phone applications," *Microwave Opt. Technol. Lett.*, Vol. 43, 7-9, 2004.
2. Yang, T. and W. A. Davis, "Planar half-disk antenna structures for ultra-wideband communications," *IEEE Antenna Propagat. Soc. Int. Symp. Dig.*, Vol. 3, 2508-2511, 2004.
3. Lee, S. H., J. K. Park, and J. N. Lee, "A novel cpw-fed ultra-wideband antenna design," *Microwave Opt. Technol. Lett.*, Vol. 44, 393-396, 2005.
4. "An asymmetrical feed arrangement for improved impedance bandwidth of planar monopole antennas," *Microwave Opt. Technol. Lett.*, Vol. 40, 156-158, 2004.
5. "Documentation in DS-UWB physical layer submission to 802.15 task group 3a," <ftp://ieeewireless@ftp.802wirelessworld.com/15/04/15-04-0137-03-003a-merger2-proposal-ds-uwband-update.doc>, Jul. 13, 2004.

TEC Measurements through GPS and Artificial Intelligence

V. Barrile, M. Cacciola, F. Cotroneo, F. C. Morabito, and M. Versaci
Univ. Mediterranea, Italy

The ionosphere is a very dynamic region that couples strongly with thermosphere and magnetosphere systems. Due to its dispersive nature, GPS differential code and carrier phases at L1/L2 frequencies can be computed. From these, the Total Electron Content (TEC) may be derived as the integral of the local electron density along the path between the satellite and the receiver. TEC, in fact, is defined as the total number electrons in the ionized plasma contained in an imaginary tube (1 m^2 cross section) between a GPS satellite and the GPS receiver. As the plasma density changes with time of day, season and solar activity, changes in TEC reflect of near-Earth space dynamics. The amount of TEC is very important because it provides two-dimensional cross-section maps of the ionosphere's electron density, with significant improvements in: mono-frequency satellite measurement; GPS and SAR imagery of geophysical phenomena (volcano deformations or subsidence detection); detection of ionospheric disturbances like geomagnetic storms, ionospheric scintillation and post-seismic perturbation, with space weather implications.

Nowadays, Kalman filters and stochastic estimations are used to calculate TEC, in order to obtain empirical ionospheric model. In our work, a new solving method is proposed; it involves Artificial Intelligence algorithms and structures in order to improve calculation performances and to reduce calculation elapsed times.

Reliability and Availability of GPS Measures in Airport Landing Systems

V. Barrile, M. Cacciola, and F. Cotroneo
University “Mediterranea” of Reggio Calabria, Italy

Abstract—In the last decades, the modern airports have considerably increased the traffic to manage. Consequently, the requirement of technological solutions in order to control vehicles and airplanes in relevancy areas (such as parking area, taxiways and runways) is increased. Among various considered solutions, the more efficient ones use Global Positioning System receivers to establish location of moving objects into the airport. Thanks to this solution, it is possible to increase both the efficiency in runway usage and the safety in ground movements. Nevertheless navigational systems like Galileo or GLONASS cannot be considered as “high availability systems”. For examples, positioning service can be interrupted by unintentional radiofrequency interferences, or terrorist attacks through techniques known as “antenna jamming” and “code contamination”. In this paper, these problems are analyzed in the context of airplane ground control, and a secure system is suggested. Especially, technical solutions are adopted in navigational routines using Global Positioning System receivers, in order to improve reliability and security, and above all to guarantee a narrow range of variation for positioning for the whole necessary time.

1. Introduction

The most critical phase in a flight is surely the landing; therefore it is necessary to increase the safety of the aerial transportations, above all civil ones, by usage of some tools which aids the pilot during the landing phase, especially in condition of low visibility. The landing instrumentation used to assist pilots or integrated in an automatic landing systems offers different performances (precision, reliability, low latency of calculation) which are compatible with specific climatic conditions. Just to be able to well classify the different levels of risk, the International Civil Aviation Organization (ICAO) defines three categories of visibility for landing civil aircraft [1]:

1. Category I—Decision Height not lower than 200 ft and Runway Visual Range (RVR) not less than 1800 ft with appropriate runway lighting; Decision Height (DH) is the height above the runway at which the landing must be aborted if the runway is not in sight;
2. Category II—DH not lower than 100 ft and RVR not less than 1200 ft; the pilot must see the runway above the DH or abort the landing,
3. Category III - This category is subdivided into:
 - IIIA: DH lower than 100 ft and RVR not less than 700 ft;
 - IIIB: DH lower than 50 ft and RVR not less than 150 ft;
 - IIIC: Zero visibility, no DH or RVR limits.

In comparison to the traditional systems for landing assistance (i. e., Instrument Landing Systems, INS, and the Microwave Landing Systems), Satellite Landing Systems (and particularly the Global Positioning System, GPS) seem to answer in a more suitable way to the requisite of precision and inexpensiveness for all the categories of employment mentioned above. Nevertheless the GPS technology has some problems related to the nature of the used signal and to the data transmission protocol from satellites to receiver. In fact, GPS receivers are susceptible to attacks exploiting interference techniques on the spread-spectrum signals (i. e., jamming), such as Denial of Service (DoS) attacks; their purpose is to make unusable a determined service, i. e., GPS service, for a particular time interval. Moreover, a hacker can modify the C/A and P codes so that the position calculated by the receiver is not correct (spoofing attack). Therefore, it is necessary to integrate the GPS system with other devices in order to eliminate these problems, which constitute an enormous limit for the adoption of the Global Position System during the landing phase. In this paper, an hybrid GPS/INS navigational system is proposed in order to avoid spoofing and jamming attacks, and to increase the precision of GPS positioning. In section 2,

jamming attacks and our GPS/INS solution approach are described; subsequently, section 3 gives a panorama of spoofing attacks and analyses our mixed protocol to avoid “code contamination”; finally, at section 4, some conclusions are pointed out.

2. Jamming Attacks and Proposed Solution Approach

The GPS signal has low power and is vulnerable to interference. The dangerous means of interference go from cheap, expendable, low-power jammers which can be widely distributed across an area of conflict, to medium and high-power ground and air-based jammers which can deny usage of GPS over hundreds of miles. The interruption of GPS positioning service by a jamming attack is particularly simple to be caused during landing phase of an airplane: in fact it is sufficient to send an interference signal on a defined location and in a defined temporal window. Since a landing assistance tool must have as principal characteristic a high availability degree for the whole period of employment, a low cost solution to the jamming vulnerability has been integrated into the GPS, the so called Inertial Navigation System (INS) [3].

INS is accomplished by an Inertial Measurement Unit (IMU) which integrates the output of a set of sensors in order to compute position, velocity, and attitude. Sensors used are gyros and accelerometers. Gyros determine angular velocity respect to inertial space, while accelerometers evaluate linear acceleration respect to an inertial frame. Integration is a simple process; difficulties are due to various encountered coordinate frames, sensor errors, and system noise. INS suffers of drift velocity errors constantly accumulated during time; therefore, an INS which operates during an appreciable length of time must be updated periodically with new positioning information. This can be accomplished by using an external navigation reference, such as GPS. An integrated GPS/INS system has advantages in terms of output rate, reliability, and accuracy. In fact:

- it is autonomous and does not rely on any other external aids or visibility conditions, and maintains the availability of navigation solution during GPS outages caused by interference, jamming, and so on;
- an optimal mixing of INS and GPS informations reduces the effect of GPS errors; therefore GPS accuracy is improved by integrated solutions;
- INS provides the full navigation state without differentiation (6 degrees of freedom, 3 translational and 3 rotational); GPS signals could be used to determine accelerations by differentiation or attitude by techniques;
- INS provides the navigation solution in real time (i.e., without latency) at rates higher than one achievable from a GPS receiver.

The integration between the two navigation systems with complementary characteristics is possible thanks to the use of a Kalman Filter. Kalman Filter is a recursive algorithm designed to compute corrections to a system based on external measurements. The corrections are weighted according to the filter’s actual estimate of the system error statistics. The derivations of the filter equations require some knowledge of linear algebra and stochastic processes. The filter equations can be unwieldy in an algebraic point of view. Fortunately, the operation of the filter can be understood in fairly simple terms. All that is required is an understanding of various common statistical measures. Kalman filtering is an extremely effective and versatile procedure for combining noisy sensor outputs to estimate the state of a system with uncertain dynamics. Kalman Filter exploits a powerful synergism between the Global Positioning System (GPS) and Inertial Navigation System (INS). This synergism is possible, in part, because the INS and GPS have very complementary error characteristics. Short-term position errors of INS are relatively small, but they have an unbounded degradation on time. GPS position errors, on the other hand, are not so good on short term, but they do not degrade with time. The Kalman filter is able to take advantage of these characteristics in order to provide a common, integrated navigation implementation with better performances than both GPS and INS ones. Kalman filter is able to combine a GPS system, having position uncertainty in the order of tens of meters, with INS system, having position uncertainty which degrades at kilometers per hour (INS); the achieved results is the so called Differential GPS (DGPS) system having position uncertainties in the order of centimeters up to meters. A key role performed by the Kalman filter is the statistical combination of GPS and INS information in order to track drifting parameters of the sensors in the INS. Therefore, the INS can provide enhanced inertial navigation accuracy during GPS signal losses; then, the improved position and velocity estimated by INS can be used to make faster the reacquisition of GPS signal.

Our proposed system uses the DGPS, because in case of jamming the initial state of INS has to be the most exact as possible. In Figure 1, a block model of the general system GPS/INS for landing help is illustrated.

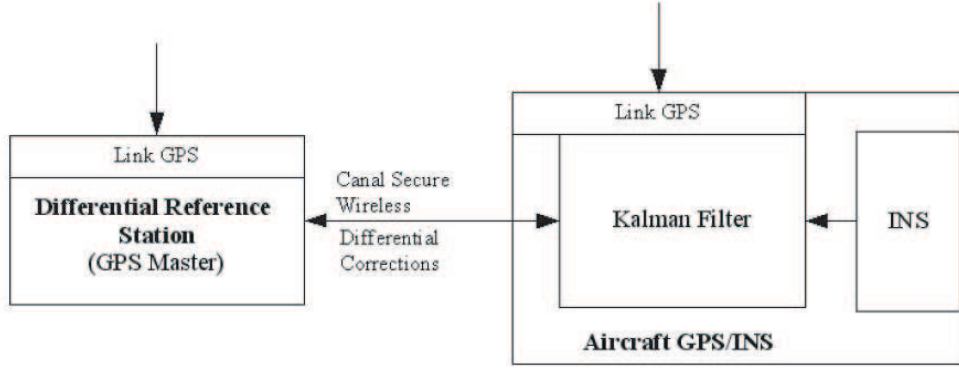


Figure 1: Integrated GPS/INS system for secure landing: it use modality of DGPS, GPS Master on the runway airport and rover over aircraft. The communication link for security is a Wireless LAN.

The master station calculates corrections to the pseudoranges of code and phase and sends them to the rover station; it applies corrections to its observations before the calculation of the position. These operations must be performed in real time, trying to minimize the latency of the whole system. The calculation of the corrections in master station uses the following equations:

$$P_m^j = \rho_m^j + E^j + c(\Delta T_m - \Delta t') + I + T \quad (1)$$

$$\Phi_m^j = \rho_m^j + E^j + c(\Delta T_m - \Delta t') - I + T + \lambda N_m^j \quad (2)$$

where P_m^j and Φ_m^j are the pseudoranges of code and phase, ρ_m^j is the master-satellite distance, E^j is ephemeris error, ΔT_m and $\Delta t'$ are respectively clock errors of master and satellite, I and T are ionospheric and tropospheric delays and λN_m^j is the phase ambiguity. By positions of j^{th} satellite from the ephemeris and master station, it is possible to calculate the master-satellite distance except than ephemeris error: $\rho_m^j + E^j$. Subtracting this quantity from P_m^j and Φ_m^j , the following equations of corrections are obtained:

$$\delta P_m^j(t_i) = P_m^j - \rho_m^j - E^j = c(\Delta T_m - \Delta t') + I + T \quad (3)$$

$$\delta \Phi_m^j(t_i) = \Phi_m^j - \rho_m^j - E^j = c(\Delta T_m - \Delta t') - I + T + \lambda N_m^j \quad (4)$$

The master station also calculates the variation of corrections for each epoch:

$$\delta \tilde{P}_m^j(t_i) = (\delta P_m^j(t_i) - \delta P_m^j(t_{i-1}))/\Delta t \quad (5)$$

$$\delta \tilde{\Phi}_m^j(t_i) = (\delta \Phi_m^j(t_i) - \delta \Phi_m^j(t_{i-1}))/\Delta t \quad (6)$$

The main calculation is the orbit determinations, which are normally drawn by the ephemeris broadcast both in the master and in the rover. Nevertheless, it is rather expensive, if it has to be repeated each second; while it is possible to calculate more quickly the orbits using the ephemeris in SP3 format. In conclusion, using DGPS with the master station on runway and a rover on airplane, and providing airplane with the typical INS instrumentation (accelerometer, gyroscope), a GPS/INS navigation system guarantees good performances in case of jamming attack. In fact, position and speed informations retrieved by INS are satisfactory to complete the landing, while GPS stops the increasing of position error calculated by INS.

3. Spoofing Attacks and Proposed Solution

The spoofing attacks are more difficulties to be realized in comparison to jamming, but at the same time they are more dangerous. In this case, in fact, the hacker replaces actual GPS data with ones compatible with the standard GPS format, inducing the pilot to consider a wrong position of airplane. Proposed solution is based on a verification system for the trajectory suggested by the system GPS/INS to the pilot. Particularly, a software/hardware computation system is placed into the control-tower; it esteems the values of parameters retrieved by GPS/INS navigation system in the following sampling instant by means of actual measures; if a strong discrepancy is obtained, the control-tower communicates to use only INS system and to disable GPS only for a few seconds, in order to avoid contemporaneous jamming attacks. An exhaustive description of system control operations can only be obtained by analyzing the timing of events which interest the airplane during the

phase of landing. In Figure 2 three operational phases are underlined, during which the modules are employed to anti-spoofing control and the control-tower develops the respective assignments.

The transmission protocol communicates the coordinates at regular time intervals. In fact, the airplane communicates its position in the WGS84 reference system at time t_i , together with the instantaneous speed. Subsequently, the control-tower esteems the value of airplane coordinates at time t_{i+1} . When the new coordinates will be received from the tower, a comparison will be made with the coordinates previously esteemed, in order to discover a spoofing attack: in this case it will be communicated to the airplane to use only the INS system. Obviously, the communication channel between control-tower and airplane must be secure; indeed, it is possible to use a wireless link similar to 802.11 b protocol or superior both for data control's communication between control-tower and airplane and for DGPS data correction's communication. Even if this technology suffers of a particular type of vulnerability, the so called "man in middle", this attack is a lot difficult to effect within the times characterizing the landing phase.

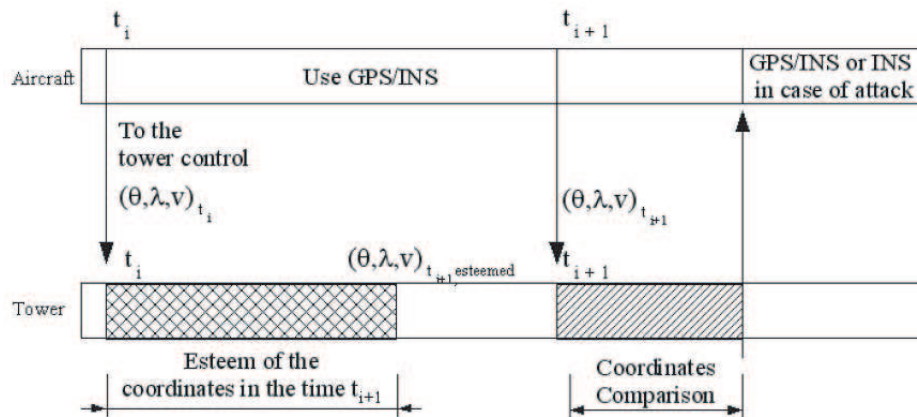


Figure 2: The aircraft communicates own coordinates to the tower in order to verify the presence of a spoofing attack.

4. Conclusions

The safety of flights is a "must" above all for civil transportation. The most dangerous phase of flight is surely the landing phase, in which the navigation systems can be subjected to jamming or spoofing attacks. In this paper, GPS and INS has been analysed; they have complementary characteristics. GPS provides an estimate of position and velocity with bounded estimation error, but it suffers of problems related to signal format and data transmission protocol. GPS uses a space-to-earth signal and the power of received signal is -160 dBW. The low power level makes GPS highly susceptible to interference and a pilot may experience short-term loss of GPS signal during the landing phase. On the other hand, INS is not dependent on the external field, but it suffers of drift velocity errors constantly accumulated during time. Therefore, the integration of these two systems is a reliable tool for helping pilots in the landing phase, above all in countries with an high risk of terrorist attacks. In this paper, a so defined GPS/INS landing-aid system has been proposed in order to avoid the jamming problem. Moreover, an infrastructure between control-tower and airplanes (based at least on 802.11 b communication protocol) has been considered in order to ensure a complete reliability of our hybrid GPS/INS system and have a secure navigational system, verifying and avoiding the presence of possible spoofing attacks.

REFERENCES

1. Federal Aviation Administrator: Advisor Circular 120-29, Advisor Circular 120-28c.
2. Brown, A., D. Reynolds, and D. Robert, "Jammer and interference location system-design and initial test results," *Proceedings of the ION 55th Annual Meeting*, 1999.
3. Stovall, S. H., *Basic Inertial Navigation*, Naval Air Warfare Center Weapons Division, California, USA, 1997.
4. Grewal, M. S., L. R. Weill., and A. P. Andrews, *Global Positioning Systems, Inertial Navigation, and Integration*, Wiley, Canada, 2001.

Electromagnetic Scattering by Rough Surfaces with Spatially Varying Impedance

M. Spivack and N. S. Basra
University of Cambridge, UK

A method is given for evaluating electromagnetic scattering by an irregular surface with spatially varying impedance. This allows examination of the effects of impedance variation and the resulting modification of rough surface scattering. Expressions are derived for the coherent field for both flat and rough surfaces, taking the form of effective impedance conditions.

Many applications of wave scattering from rough surfaces are complicated by the involvement of further scattering mechanisms. Radar propagating over a sea surface, for example, may encounter refractive index variations in the evaporation duct or spatially varying impedance due to surface inhomogeneities. This is an even greater problem in remote sensing over forest or urban terrain. The great majority of theoretical and numerical studies, most focusing on surface roughness, nevertheless treat such effects in isolation. Roughness is usually the dominant feature but impedance variation may produce further multiple scattering. Experimental validation of scattering models in complex environments remains a major difficulty, exacerbated by the lack of detailed environmental information, and it is therefore crucial to distinguish and identify sources of scattering. In addition, while numerical computation in these cases may be feasible for the perfectly reflecting surface, it can become prohibitive for more complex environments, particularly in seeking statistics from multiple realisations.

This study is motivated by these considerations. We have sought to provide an efficient means to evaluate the effect of impedance variation and its interaction with surface roughness, and to derive descriptions of the resulting coherent or mean field, for both flat and irregular surfaces.

Results have been derived by use of an operator expansion: Surface currents (from which scattered fields are determined) are expressed as the solution of an integral equation, in which the effect of impedance variation is separated. The solution is written in terms of the inverse of the governing integral operator, and provided the impedance variation is not too large this inversion can be expanded about the leading term.

Development of the Pulsed Direct Current Iontophoresis and Its Clinical Application

M. Akimoto¹, M. Kawahara², M. Matsumoto², and H. Matsubayashi²

¹Kanto Gakuin University, Japan

²I. C. I. Cosmetics Japan, Japan

Abstract—The skin is a primary area of body contact with the environment and is the route by which many chemicals enter the body. The delivery of drugs into and through the skin has been an important area of research for many years. Iontophoresis can be defined as the process of increasing the rate of penetration of ions into or through a tissue by the application of an external electric field across the tissue. Impedance spectroscopy was used to investigate the electrical response of skin to different ions, applied currents and fields. The stratum corneum shows two important electrical features. First, it tends to become polarized as an electrical field is applied continuously. Second, its impedance changes with the frequency of the applied electrical field. To avoid the counterproductive polarization, the current should be applied in a periodic manner, which is called pulsed direct current. The pulsed direct current generating iontophoretic delivery system was developed. In the state of on, charged molecules are delivered by the iontophoretic diffusion process into the skin. A non-parenteral method for the delivery of macromolecules was developed by using a pulse direct current mode iontophoretic technique.

1. Introduction

Medical diagnosis and in-patient drug monitoring rely upon the detection and quantitation of endogenous and exogenous bioactive chemicals. Currently, such analysis is predominantly based upon blood sampling which is achieved invasively via needle. The inconvenience and limitations of this procedure are well-known; patients, on the whole, would rather not be injected, the frequency and amount of sampling is constrained, successful intravenous access in geriatric and pediatric patients may be difficult, and there are risks to both patient and sampler. The potential benefits of alternative, noninvasive sampling procedures for chemical exposure assessment and continuous drug monitoring have been described. One approach involves collection, via the skin, of molecules circulating systemically. A major difficulty, however, with this idea is the characteristically very slow and variable passive permeation rates of chemicals across the skin. Indeed, experiments examining the outward migration of theophylline revealed little correlation between sampled amounts and drug levels in the body. Additionally, it was necessary to collect samples over extended periods of time, a significant potential drawback. To circumvent these problems, the application of iontophoresis to enhance sampling efficiency has been examined. Iontophoresis employs an electrical potential gradient to promote the penetration of ionizable molecules across the skin [1–3]. The current uses of the technique are the treatment of dermatology and aesthetic dermatology. In this paper, we have investigated the efficiency of a pulse waveform in the iontophoretic delivery of insulin to achieve blood glucose control and compared the results with a simple direct current iontophoretic delivery system.

2. Theoretical Consideration

The skin of an average adult body covers a surface area of $\sim 2\text{m}^2$ and receives about one-third of the blood circulating through the body. It is one of the most readily accessible organs on the human body. The skin is divided into three layers: the epidermis, the dermis, and the subcutaneous tissue. The epidermis is the outermost portion of the skin and is composed of stratified squamous epithelium. The epidermal thickness varies from $50\ \mu\text{m}$ on the eyelids to 1.5mm on the palms and soles. The innermost layer of the epidermis consists of a single layer of cuboidal cells called basal cells. These cells differentiate and migrate towards the skin surface. The outer layer of the epidermis is called the stratum corneum, which is composed of flattened and dead cells. As they migrate to the skin surface, the cells become more stratified and finally form the cornified layer of the stratum corneum. The skin is known to produce a large impedance to charged molecules as they are driven through the skin by an applied electrical field. The electrical properties of the skin are known to be dominated by the least conductive stratum corneum. Under the influence of electric current, ionic species or charged molecules are driven across the skin, possible through the shunt pathways or intercellular spacing in the stratum corneum, since the skin is likely to be perturbed during iontophoresis, which may remove or disrupt

the intercellular lipids, resulting in the formation of artificial shunts. Iontophoresis facilitated skin permeation flux of an ionic species can be described by an equation consisting of the following three components [4–5]:

$$J = J^p + J^e + J^c \quad (1)$$

where the first term on the right-hand side is the passive skin permeation flux, given by

$$J^p = K_s D_s \frac{dC}{h_s} \quad (2)$$

the second term is electric current driven skin permeation flux

$$J^e = \frac{Z_i D_i F}{RT} C_i \frac{dE}{h_s} \quad (3)$$

and the last term is the convective flow driven skin permeation flux

$$J^c = k C_s I_d \quad (4)$$

in which K_s is coefficient for interfacial partition from donor solution to stratum corneum, C_i is donor concentration of ionic species, C_s is concentration in the skin tissue, dE/h_s is electric potential gradient across the skin, dC/h_s is concentration gradient across the skin, D_i is diffusivity of ionic species I in the skin, D_s is diffusivity across the skin, I_d is current density applied, Z_i is electric valence of ionic species I , k is proportionality constant, F is Faraday constant, T is absolute temperature, and R is gas constant. This equations describes the flux of an ion under the influence of both a concentration gradient and an electrical field.

Table 1: Some representative iontophoretic delivery systems.

Iontophoretic system	Drug delivery mode
<i>Direct current mode</i>	Continuous drug delivery under constant intensity of direct current
<i>Pulse current mode</i>	
(a) Depolarizing pulse Iontophoresis system	Continuous drug delivery under constant application of pulse current
(b) Periodic iontotherapeutic system	Programmed drug delivery under periodic applications of pulse current with constant intensity

Essentially, two types of iontophoresis have been investigated: the earlier one uses a simple direct current mode, while the more recent one utilizes the pulsed direct current mode in shown Table 1. An iontophoretic drug delivery system is composed of four basic components including a battery, control circuitry, electrodes, and reservoirs. The component configuration is schematically illustrated in Figure 1. The battery supplies the required energy to power the control circuitry which, subsequently, controls the electric potential applied to the electrodes. Because drug delivery is roportional to the current flowing through the body, most iontophoretic transdermal drug delivery control circuits utilize some type of current source to compensate for the difference in skin resistance from person to person. A battery and a single resistor is a simple current regulator, but regulation is effective for only small resistance variations. Active current regulators automatically adjust their operating characteristics in response to a broader range of resistances and therefore are preferred for iontophoretic transdermal drug delivery applications since the resistances from person to person or from site to site can vary significantly. The electrodes of an iontophoretic device are in direct electrical contact with the reservoirs, and together they determine the electrochemical reactions that occur at the anode and cathode. These reactions are particularly important to

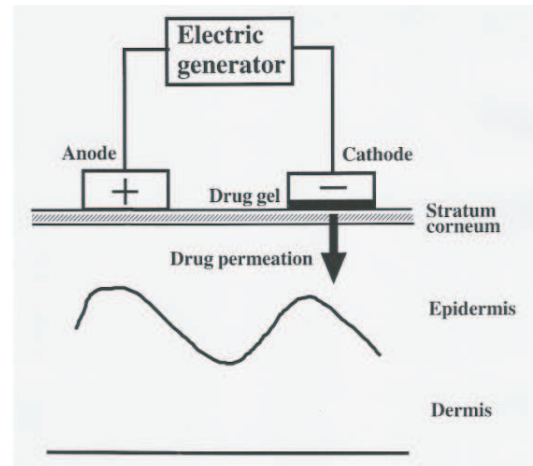


Figure 1: Schematic illustration of the major components of an iontophoresis system.

consider when designing iontophoretic devices for the delivery of drugs over extended periods of time. A better choice of electrode materials would be titanium or silver for the anode and chloridized silver for the cathode.

3. Materials and Methods

Tissue samples were obtained from freshly rats skin. All tissues of exactly known time history were prepared in the same way. A cylinder of diameter corresponding to the diameter of the electrode was excised from the bulk of the test tissue. It was then inserted into a plastic tube and a microtome was used to cut tissue discs of the desired thickness equal to the distance between the electrodes. The dielectric measurements were performed using automatic swept-frequency network and impedance analyzer. The frequency range 5 Hz to 10 MHz was covered by an HP-4192A impedance analyzer. Open-ended co-axial probe were used to interface the measuring equipment with the samples in all cases. The probe is characterized by a fringing capacitance and conductance which are functions of its physical dimension and can be measured with the impedance analyzer. In addition there are stray capacitive and inductive elements that have to be normalized. Figure 2 is a schematic diagram of the experimental arrangement [6]. For each set of measurements new samples were excised from the bulk of the tissue, which was sealed to avoid tissue drying and stored at ambient temperature during the measurement session.

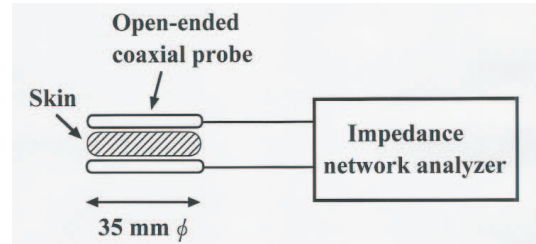


Figure 2: Schematic diagram of the measuring system.

4. Results and Discussion

The condition inside the tissues when adding an electric field to the tissues becomes the index that the complex permittivity of the tissue is important. The real component corresponding to the permittivity and the imaginary component, known as the dielectric loss, corresponds to the dissipative loss associated with the movement of polarisable charges in phase with the electric field. This shows that, as a dielectric dispersion is traversed by changing the frequency of measurement, the change in conductivity is directly proportional to the change in permittivity. This follows from the fact that the total energy in the field is constant and must either be stored or dissipated by the system with which it interacts. The dielectric properties of skin show considerable variability over different parts of the body. The average electrical properties of skin in the range 5 Hz–1 MHz are shown in Figure 3. An interpretation of these properties was approached via a consideration of the inhomogeneous structure and composition of skin and of the way in which this varies from the skin surface to the underlying dermis and subcutaneous tissues. The dielectric properties of skin are largely determined by the stratum corneum, which has a thickness of some 15 μm and consists largely of dead cells [7–9]. As for the complex permittivity, the characteristic to become minimal around 50 kHz was measured.

It may be noted that skin possesses a relatively weak α dispersion, and this relative lack of a significant dispersion in the frequency range 1 Hz–100 kHz is plausibly ascribed to the dead nature and low conductivity of the stratum corneum. It was tentatively suggested that the origin of these dispersions lay in the stratum corneum and was associated with the relaxation of ions surrounding the corneal cells. It is worth drawing attention to the fact that the electric impedance of those parts of the skin at which the points and meridians of acupuncture are located is significantly less than that of the surrounding tissue, a fact which may be presumed to be of diagnostic value and may plausibly underlie the mechanism by which signals are transmitted around the body by means of the meridians of acupuncture. Many therapeutic and diagnostic techniques rely upon the application of electrical fields or

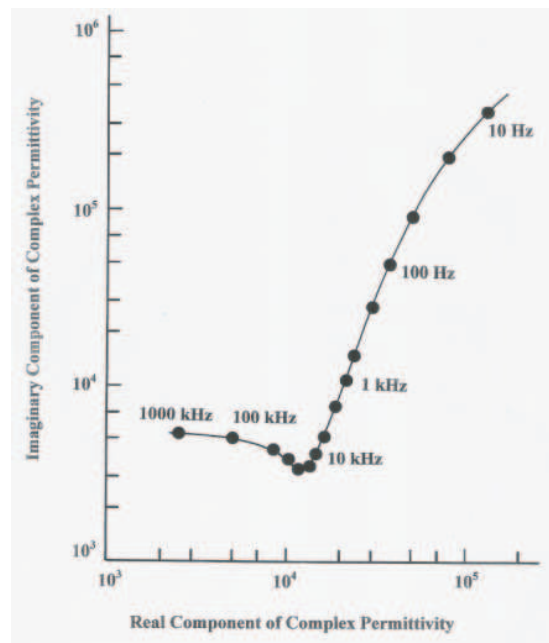


Figure 3: A typical example of the dielectric constants of skin as a function of frequency.

the measurement of electrical properties. Since skin tissue often constitutes the interface between the biological and electronic parts of the system, its dielectric properties are of some interest and importance. It is worth drawing attention to the fact that the electric impedance of those parts of the skin at which the points and meridians of acupuncture are located is significantly less than that of the surrounding tissue, a fact which may be presumed to be of diagnostic value and may plausibly underlie the mechanism by which signals are transmitted around the body by means of the meridians of acupuncture. Therefore, the complex permittivity is the important index that the energy absorption which is consumed in the tissue can be discussed.

Skin manifests large impedance to charged molecules which are driven through the skin under an applied electrical field. The electrical properties of the skin are dominated by the stratum corneum which is considered to be the least conductive layer of the skin. Stratum corneum consists of multilayers of cornified cells. These electrically insulated horny cells are continuously replenished by the slow upward migration of cells from the basal cell layer of the stratum germinativum. An analogous equivalent circuit of skin impedance is shown in Figure 4. It consists of a resistor, R_{sc} , and a capacitor, C_{sc} , existing in parallel in the stratum corneum, which is then in series with the resistor, R_{vs} , in the viable skin. The magnitude of R_{sc} is rather large, and can range from 10–20 $k\Omega cm^2$ in animal skin to 100–5000 $k\Omega cm^2$ in human skin, while

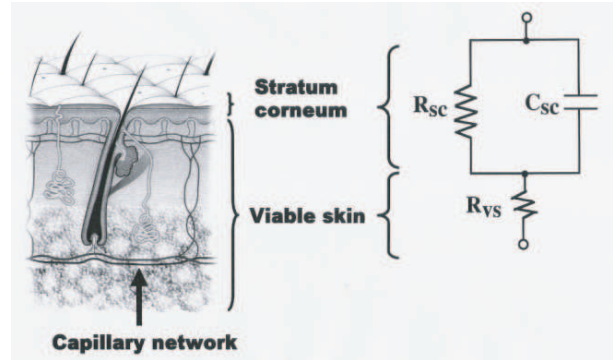


Figure 4: Diagrammatic illustration of the analogue equivalent circuit of skin impedance.

R_{vs} is relative small in magnitude and is in the range of 0.1–1.0 $k\Omega cm^2$. The stratum corneum shows two important electrical features: first, it is polarized by the electrical field, and second, its impedance changes with the frequency of the applied electrical field. When an electrical field with direct current is applied in a continuous manner to the skin, an electrochemical polarization develops rapidly in the capacitor. It often operates against the applied electric field and greatly decreases the magnitude of effective current across the skin.

To avoid the polarization of the stratum corneum, a pulse direct current can be used [10]. The pulse mode is a direct current voltage which periodically alternates with the “on” and “off” of the applied voltage in Figure 5. In the state of “on”, charged molecules are forced into the skin and the stratum corneum soon becomes polarized; while in the state of “off”, no external stimulation is present and the stratum corneum becomes depolarized. The on/off ratio controls the proportion for polarization and depolarization process in each cycle. The current output generators were built in-house. The pulsed-current unit was designed to provide adjustable peak voltages from 0 to 20 V and variable frequency from 0 to 300 kHz. The wave form used in the pulsed-current unit is also shown in Figure 5. The on/off ratio or the percent duty could be varied from 0 to 70%. This unit had 15 channels and a display that provided the average current readout for each channel. This average current readout is the current averaged over the cycle. At a setting of 40 kHz duty, for example, the duration of each pulse would be 25 μs , but at a setting of 30% duty, the pulse would be on for 7.5 μs and off for 17.5 μs . In some experiments, a pulsed-current unit with a single output channel and a fixed frequency and percent duty was used. When an ideal on/off ratio is selected, every new cycle starts with no residue polarization left in the skin from the previous cycle, i.e., the effect of polarization is eliminated.

The energy (E) required to overcome the penetration barrier, stratum corneum, can be expressed by:

$$E = \int [V(t)i(t)]dt = \int [i(t)^2 R_t(t)]dt \quad (5)$$

where $V(t)$ and $i(t)$ are the voltage and current applied respectively and R_t is the impedance of the skin. As can be seen from Eq. 5, less energy will be required to overcome the barrier when the skin impedance is reduced. This may be achieved by applying the current with proper frequency and on/off ratio. Therefore, it is essential to select optimum pulse mode parameters to attain the best facilitating effect of iontophoresis for a particular drug or a dosage form.

Diabetes mellitus is a chronic systemic disease in which the body either fails to produce or fails to respond to the glucose regulatory hormone insulin. Insulin is required in order for cells to take up glucose from the blood, and in diabetics, a defect in insulin signaling can give rise to large fluctuations in blood glucose levels unless proper management techniques are employed. Insulin, a protein hormone containing 51 amino acid residues, has a molecular weight of approximately 6,000 daltons and an extremely short biological half-life of

less than 30 minutes. In healthy humans, it is secreted by beta cells in the Langerhans islet of the pancreas in response to an increase in blood glucose level to facilitate the process of glucose utilization for either energy or storage. Inpatients with diabetes mellitus, however, the capacity of the pancreas to supply insulin in response to the increase in blood glucose level is impaired. For the control of diabetes mellitus, insulin must be supplied externally by subcutaneous injection at a dose of 10–20 units three to four times a day. Experiments were conducted in a skin to study the feasibility of facilitating the transdermal delivery of insulin across the freshly excised abdominal skin of rats by applying iontophoresis with a pulsed direct current. The results demonstrated that the skin permeation rate of insulin thus applied is enhanced substantially as compared to that achieved by passive diffusion alone. The insulin data summarized in Figure 6 were generated using the iontophoresis shown in Figure 5. The use of iontophoresis results in the typical sigmoidal dependence of receptor concentration on time. The time required to achieve a steady-state receptor concentration is determined by the receptor volume and flow rate of the receptor solution. For the in vivo conditions used in the insulin study, time to achieve a steady-state concentration was about 2 hours for all currents, as shown in Figure 6.

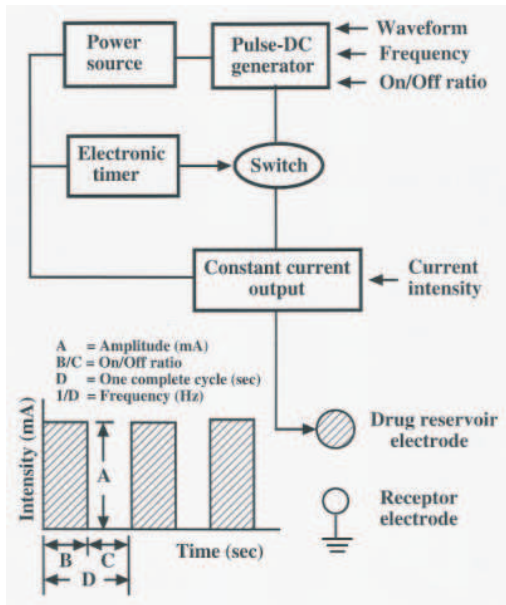


Figure 5: Diagrammatic illustration of the transdermal periodic iontophoresis system. Diagram of a pulse waveform profile, where A is the amplitude of a current intensity (mA), B/C are the on/off ratio, D is the duration (s) of a complete cycle and so 1/D is the frequency.

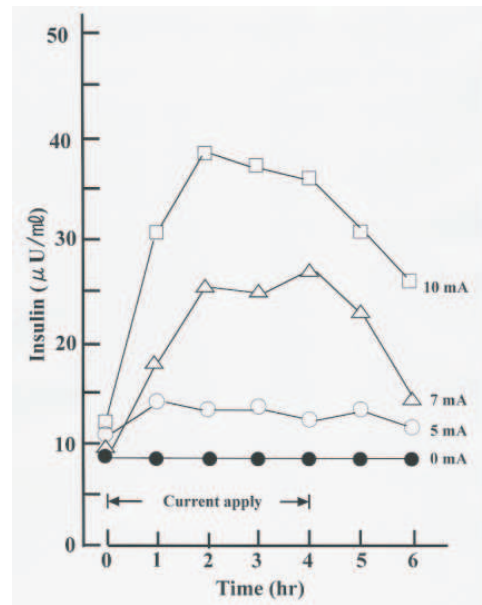


Figure 6: In vivo skin permeation profiles of insulin under the iontophoresis facilitated permeation by the pulse current.

The cumulative amount of insulin permeating through the skin increases with time during the period of transdermal periodic iontotherapeutic system treatment and gradually returns to the skin permeation profile by passive diffusion after termination of the treatment. Also plotted in Figure 6 for comparison is the rate profile of insulin permeation. Analysis of the skin permeation rate profile suggests that the pulsed direct current iontophoresis facilitated transdermal transport of drug molecules consists of four phases: (i) the facilitated absorption phase, in which the skin permeation of drug molecules is enhanced by iontophoresis treatment and the skin permeation rate linearly increases with the time of treatment; (ii) the equilibrium phase, in which the skin permeation rate has reached a plateau even though iontophoresis treatment is continuously applied; (iii) the desorption phase, in which the skin permeation rate decrease lineally with time immediately after the termination of iontophoresis treatment and the drug molecules already delivered into the skin tissues are desorbed into the receptor solution; and (iv) the passive diffusion phase, in which the skin permeation rate returns to the baseline level as defined by passive diffusion. The transdermal periodic iontotherapeutic system facilitated skin permeation rate of insulin was observed to increase linearly with the current density of pulsed direct current applied, but in a non-linear manner with the duration of transdermal periodic iontotherapeutic

system application time. The therapeutic response of insulin obtained in the present study indicates that, in the presence of a facilitated transport, it may be possible to topically administer high molecular weight substances, including other peptides and/or proteins, for systemic therapy. The present work has demonstrated that the iontophoresis technique may provide a convenient means for the systemic delivery of insulin without the use of a hypodermic needle. The feasibility of optimizing the plasma concentration of the drug by either controlling the time of application and/or regulating the magnitude of current, or alternatively, by the use of a pulse current rather than a direct current, needs further investigation.

5. Conclusions

A non-parenteral method for the delivery of macromolecules such as insulin was developed by using a pulse direct current mode transdermal iontophoretic technique. The intensity of current, frequency, on/off ratio and mode of waveform were found to play an important role in the transdermal iontophoretic delivery of insulin. More extensive investigations on various aspects of this system are necessary to obtain optimum parameters of pulse direct current mode for transdermal iontophoretic delivery of dermatology and cosmetic science.

REFERENCES

1. Banga, A. K. and Y. W. Chien, "Iontophoretic deliver of drugs: fundamentals, developments and biomedical applications," *Controlled Release*, Vol. 7, 1–24, 1988.
2. Banga, A. K. and Y. W. Chien, "Hydrogel-based iontophoretic delivery devices for transdermal delivery of peptide/protein drugs," *Pharm. Res.*, Vol. 10, 697–702, 1993.
3. Merclin, N., T. Bramer, and K. Edsman, "Iontophoretic delivery of 5-aminolevulinic acid and its methyl ester using a carbopol gel as vehicle," *Controlled release*, Vol. 98, 57–65, 2004.
4. Keister, J. C. and G. B. Kasting, "Ionic mass transport through a homogeneous membrane in the presence of a uniform electric field," *J. Membrane Sci.*, Vol. 29, 155–167, 1986.
5. Hiemenz, P. C., *Principles of Colloid and Surface Chemistry*, Marcel Dekker, New York, 1986.
6. Egawa, M., L. Yang, M. Akimoto, and M. Miyakawa, "A study of electrical properties of the epidermal stratum corneum," *Progress In Electromagnetics Research Symposium*, Boston, Massachusetts, 596, 2002.
7. Dissado, L. A., "A fractal interpretation of the dielectric response of animal tissues," *Phys. Med. biol.*, Vol. 35, 1487–1503, 1990.
8. Sapoval, B., "Fractal electrodes and constant phase angle response, exact examples and counter-examples," *Solid State Ionics*, Vol. 25, 253–259, 1987.
9. Gabriel, S., R. W. Lau, and C. Gabriel, "The dielectric properties of biological tissues: II. Measurements in the frequency range 10 Hz to 20 GHz," *Phys. Med. biol.*, Vol. 41, 2251–2269, 1996.
10. Bagniefski, T. and R. R. Burnette, "A comparison of pulsed and continuous current iontophoresis," *Controlled release*, Vol. 11, 113–122, 1990.

Design of Reduced-size Branch-line Couplers with Series Capacitors

T. Kawai, Y. Kokubo, and I. Ohta
 University of Hyogo, Japan

Branch-line couplers are widely used in microwave and millimeter-wave circuit systems such as balanced mixers, balanced amplifiers, phase shifters, and etc. Since conventional couplers designed based on the distributed circuit theory tend to waste chip area in MICs or MMICs, especially at low frequencies, thus many research efforts have been devoted to reduce the size of couplers. Here, we treat branch-line couplers with series capacitors at each input/output port as shown in Fig. 1(a) and design reduced-size couplers based on the equivalent admittance approach. Fig. 1(b) exhibits the theoretical scattering parameters for the compact coupler that the electrical length of branchlines is 60° . As shown in this figure, the fractional bandwidth is about 10% for -20 dB return loss. This value is comparable to that of the conventional branch-line coupler. The validity of this design technique is demonstrated by electromagnetic simulator (Sonnet em) assuming that the glass substrate with dielectric constant of 4.8 and thickness of 0.5 mm, respectively. Fig. 2 shows the circuit pattern of simulation for the proposed coupler designed at center frequency of 3 GHz. In this circuit, input/output ports and branch-lines are constructed of coplanar waveguides (CPWs). Metal- Insulate-Metal (MIM) capacitor is constructed with the air gap ($Gap = 3 \mu\text{m}$, $area = 0.3 \text{mm}^2$) under the CPW center conductor near each port junction. In order to avoid the parasitic slot-line mode, air bridges are added near the junctions. Simulation results given by plots in Fig. 1(b) generally agree with the theoretical results. We demonstrate that the size reduction of about 50% can be achieved with maintaining the property comparable to that of the conventional couplers. Experiment verifications will be our feature works.

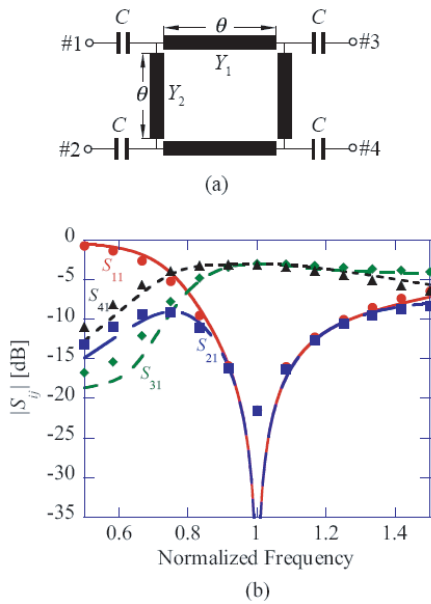


Figure 1: (a) Circuit construction and (b) frequency characteristics of scattering parameters of branch-line coupler with series capacitors ($Y_1 = 0.50, Y_2 = 0.35, C = 0.83, \theta = 60^\circ$).

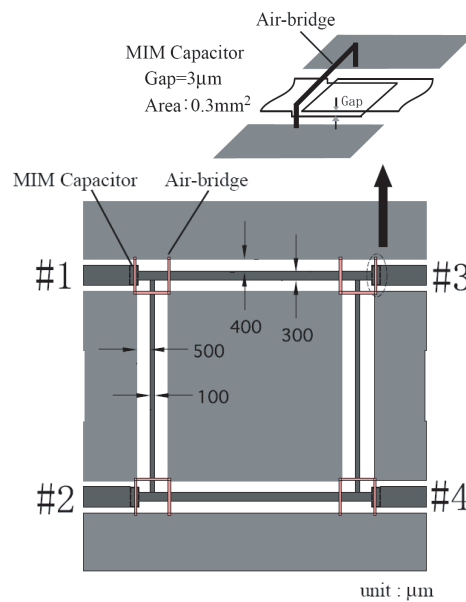


Figure 2: Circuit pattern of a proposed coupler.

Plane Wave Scattering by an Array of Pseudochiral Cylinders

M. Polewski, R. Lech, and J. Mazur
Gdansk University of Technology, Poland

This paper presents the analysis of electromagnetic plane wave scattering by cylindrical objects made of pseudochiral material located in free space.

Presented approach is based on the Iterative Scattering Procedure (ISP) [1] and allows to define the total scattered field from arbitrary configurations of cylinders. To take into account practical applications two layered cylindrical object is defined. As shown in Fig. 1 the inner dielectric or metallic core is covered with the pseudochiral material. For configuration from Fig. 1 assuming TM^z excitation and homogeneity of the field along z axis, the following wave equation is obtained [1, 2].

$$\rho \frac{\partial}{\partial \rho} \left(\rho \frac{\partial E_z}{\partial \rho} \right) + k_o^2 \varepsilon_z \mu \rho^2 E_z + \frac{\mu}{\mu_\rho} \frac{\partial^2 E_z}{\partial \phi^2} = 0 \quad (1)$$

It is important to note that the elements $\varepsilon_z \neq \varepsilon$ and $\mu_\rho \neq \mu$ indicate the pseudochirality effect in the considered cylinder.

The results of numerical experiment for the configuration of three pseudochiral cylinders have been presented in Fig. 2. It can be noticed that the level of side lobes for pseudochiral cylinders (Fig. 2b) decreases significantly in comparison to the configuration of dielectric posts (Fig. 2a).

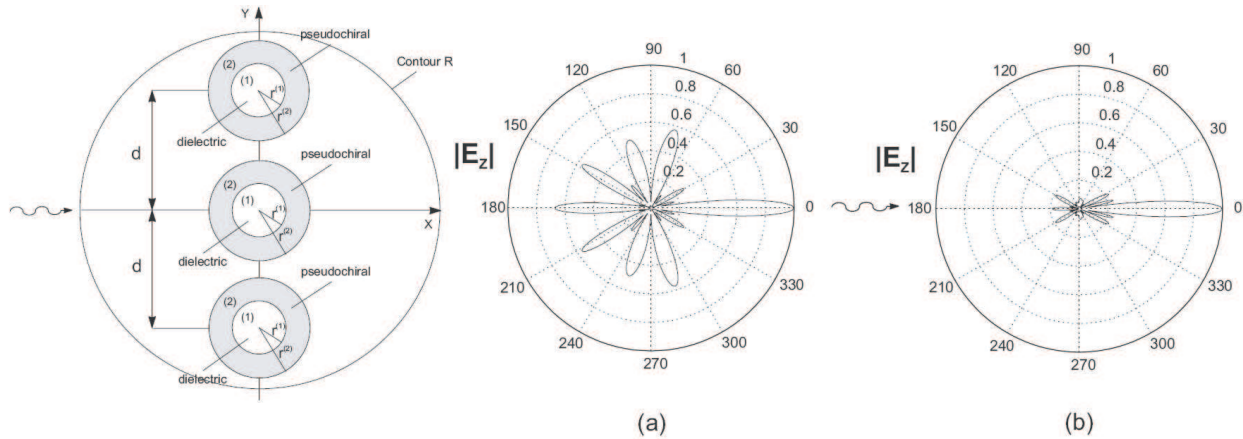


Figure 1: Pseudochiral cylinder geometry.

Figure 2: Scattering characteristics of $|E_z|$ for TM^z excitation from three pseudochiral cylinders. Plane wave excitation along x -axis direction. Dimensions: $r^{(1)} = 0.4\lambda$, $r^{(2)} = 0.75\lambda$, $R = 3\lambda$, $d = 2\lambda$, $\rho = 100\lambda$, $M = N = 26$: (a) dielectric cylinders: layer (1) $\varepsilon^{(1)} = 2$, layer (2) (host medium) $\varepsilon^{(2)} = 4$, $\varepsilon_z^{(2)} = 4$, (b) pseudochiral cylinders: layer (1) $\varepsilon^{(1)} = 2$, layer (2) $\varepsilon^{(2)} = 4$, $\varepsilon_z^{(2)} = 9$, $\mu^{(2)} = 1$, $\mu_\rho^{(2)} = 1.5$.

REFERENCES

1. Polewski, M. and J. Mazur, "Scattering by an array of conducting, lossy dielectric, ferrite and pseudochiral cylinders," *Progress in Electromagnetic Research, PIER* 38, 283310, 2002.
2. Engheta, N. and M. M. Saadoun, "Novel pseudochiral or Ω -medium and its applications," *Proc. of PIERS91*, Cambridge, MA, 339, July 1991.

Electromagnetic Field for Randomly Oriented Particle Located in Laser Beam

Y. P. Han and H. Y. Zhang
Xidian University, China

There are a lot of practical applications involving particle, such as particle size measurements using a phase Doppler instrument, light scattering by aerosols in atmosphere, trapping the particle in laser tweezers, the absorption in the human head of electromagnetic waves emitted by hand phones and the effect of radomes (spheroidal dielectric covers) on radar and communications antennas. Many investigations on the scattering from particle have been carried out. GLMTs describe the interaction between an arbitrary shaped beam and a class of scatterers exhibiting a regular surface. In GLMTs, the most difficult task concerns the description of the illuminating beam. Gouesbet et al. have provided approaches for expansions of the incident shaped beam propagating parallel to the coordinate axis (i.e., an off-axis beam).

In this paper, we provide the description of the arbitrarily shape beam, for example, a plane wave or a Gaussian beam, for any angle incidence by virtue of the Generalized Lorenz-Mie theory. The incident beam is decomposed into an infinite series of elementary constituents, such as partial wave or plane waves, with amplitudes and phases given by a set of beam-shape coefficients. We derive the transformation of spherical vector wave functions with reference to the two different spherical coordinate systems under rotated translation and obtain the general expression of beam shape coefficients $g_{n,TE}^{ms}$, $g'_{n,TE}{}^{ms}$, $g_{n,TM}^{ms}$, $g'_{n,TE}{}^{ms}$ for the randomly oriented scatterer.

Once the beam-shape coefficients in coordinates are determined, the solution of scattering for arbitrary shaped beam by a particle is obtained by means of the method of separation of variables. The fields are expanded in the terms of the spherical vector wave functions. The unknown coefficients of scattered and internal electromagnetic fields are determined by solving a system of linear equations derived from the boundary conditions. The exact analytic solution of scattering from a randomly oriented axisymmetric particle with an arbitrarily shaped beam illumination can be obtained by means of the method of separation of variables. Also, the numerical results for the beam scattering properties for particle is given. The associated code, developed under Matlab, is suitable for computing the scattering properties of the randomly oriented particles, allowing one to extensively investigate the dependence of scattering properties on the particle size, shape, refractive index, magnitude and location of beam waist. This study is suggestive and useful for interpretation of electromagnetic scattering phenomena from oriented particles.

Corrector Packaging for Heating inside a Domestic Microwave Oven

A. Rhattoy and S. Bri

Université Moulay Ismail Meknes, Morocco

M. Audhuy-Peudeceder

ENSEEIH-T-INPT, France

In this paper, we demonstrate that an adapted packaging improves the microwave cooking. The electromagnetic and thermal functions of the packaging are studied. This applicator is constituted of a slot array or a metallic bar array which is positioned on a metallic box filled with an alimentary product. The slot array purpose is to homogenise the power distribution inside the metallic box and to minimise the coupling degree between the product, the microwave oven and the generator. It is possible to control the electromagnetic fields by means of the packaging that becomes a second oven in the first oven. In this case the field calculation is realised by the Finite Element Method. We have calculated the width of the slots, the distance between them and the height of the slot array in relation to the product according to the following criteria: Electromagnetic fields inside the product should be uniform and independent of the fields in the oven, the input impedance of the cavity should be constant wherever the position of the product in the oven.

A WEB Application for Electromagnetic Structures

A. S. B. Lopes, F. M. Sales Junior, and J. R. S. Oliveira
CEFETRN/NUTEL, Brazil

Several structures in electromagnetic applications were studied along the last decades and the results have been published in reports, papers and magazines. With the success of Internet applications, it's important to think how we could use it to permit users to resolve some simple problems using a browser to inform some characteristics of a structure and receive the result of his research. Structure like transmission lines, antennas, planar circuits are, sometimes, analyzed using approximate equations that are enough to some applications. So, we can use them to construct a WEB interface to receive the data and to show the results.

In this paper, a WEB interface is constructed to solve problems of transmission line, antennas and planar circuits and used as a tool to analysis and synthesis of such structures. The objective is use, initially, closed equations to characterize some transmission lines presenting results for characteristic impedance, resistance, inductance, capacitance, loss conductor, loss in dielectric and attenuation.

In the analysis of antennas, some types are considered, like monopole, dipole, helicoidal, yagi, microstrip and others. The variables to be analyzed are resonant frequency, gain, radiation pattern and quality factor. It is important in a WEB application, the graphical behavior of some electrical parameters, like frequency versus length or height.

Other application of special importance for designers is the synthesis of transmission lines, antennas and circuits. The WEB interface allows the filling in some fields with the desired electric parameters and the output presents the physical characteristics of such structure.

This kind of WEB applications is been projected to be also used as a didactic tools for teaching electromagnetic concepts to the CEFETRN's students in analysis of electromagnetic concepts and some projects. The final objective is to obtain a portal that grows with the addition of new devices. This growth can be done by any person involved in the project in any place of the world using the WEB management tool.

Computation of Resonant Frequencies of Any Shaped Dielectric Resonators by CFDTD

A. Shahvarpour and M. S. Abrishamian
K. N. Toosi University of Technology, Iran

Abstract—Dielectric resonators (DR) have helped achieving the miniaturization of many active and passive microwave components, such as oscillators, filters and antennas. Nowadays they are used widely in mobile telecommunications and optical instruments such as optical couplers and filters. To design such components, designers must have the knowledge of predicting the shape and resonant frequency response of usable dielectric resonators. Numerical methods such as Method Of Moment (MOM), Finite Element Method (FEM) and Finite Difference Time Domain (FDTD), are useful tools for simulating those problems. The MOM & FEM are usually in frequency domain and we need to inverse a large matrix to solve the problem. Fortunately, FDTD is in time domain and by one run, we can have a large bandwidth response of our system. We have prepared a program code for determining resonant frequencies of DRs by using Conformal Finite Difference Time Domain (CFDTD) which is used for curved surfaces such as cylindrical and spherical shapes in Cartesian coordinate. In this paper, first, we present the simulation of resonant frequencies of cylindrical dielectric resonator which its results can be compared with reference results. In proceeding, computation of resonant frequency response of a thin dielectric spherical layer that can be useful for improving the achievement of Whispering Gallery Modes, which are produced in spherical DRs, will be considered.

1. Introduction

Dielectric resonators are used widely in mobile telecommunications and optical instruments, such as antennas, filters and couplers. Knowledge of predicting the shape and resonant frequency response of usable dielectric resonators is very important for engineers to design these telecommunication systems. Finite Difference Time Domain method is one of the numerical methods and even the most useful one for determining resonant frequencies of DRs, because by one run, we can have a large bandwidth response of our system.

In this work, we have prepared a code program for determining resonant frequencies of DRs by FDTD method, and for cases with curved surfaces such as cylindrical and spherical shapes we have used Conformal FDTD to reduce the error introduced by staircasing of surfaces that are not precisely aligned with major grid planes. To achieve such a goal, we have used the method suggested by Ref. [1] for simple structures. We have expanded that method for Yee cells which contain three or more layers of dissimilar dielectrics. We have used this method for simulation of thin layer dielectric curved surfaces, such as shelled spheres, that can be useful for improving the achievement of Whispering Gallery Modes.

The analytic method for computation of resonant frequencies of any spherical layers, which is used for verification of numerical method, is discussed in section 2. The CFDTD method applied for computation of resonant frequencies of any shaped DRs is in section 3 and finally in section 4, results of simulating are compared with analytic method and Ref. [4].

2. Analytical Computation of Resonant Frequencies of Multi Spherical Shells

In this section we only consider a dielectric sphere with a single coating layer. We use the Mie theory to compute the resonant frequencies. According to Ref. [2], we introduce two vectors \mathbf{M} and \mathbf{N} which correspond to TE and TM spherical modes.

$$\mathbf{M} = \mathbf{M}_e + j\mathbf{M}_o \quad (1)$$

$$\mathbf{N} = \mathbf{N}_e + j\mathbf{N}_o \quad (2)$$

where

$$\mathbf{M}_{omn} = \frac{m\hat{a}_\theta}{\sin(\theta)} Z_n(\beta r) P_n^m(\cos(\theta)) \cos(m\varphi) - \hat{a}_\varphi Z_n(\beta r) \frac{\partial}{\partial \theta} P_n^m(\cos(\theta)) \sin(m\varphi) \quad (3)$$

$$\mathbf{M}_{emn} = -\frac{m\hat{a}_\theta}{\sin(\theta)} Z_n(\beta r) P_n^m(\cos(\theta)) \sin(m\varphi) - \hat{a}_\varphi Z_n(\beta r) \frac{\partial}{\partial \theta} P_n^m(\cos(\theta)) \cos(m\varphi) \quad (4)$$

$$\begin{aligned} \mathbf{N}_{omn} &= \hat{a}_r \frac{n(n+1)}{\beta r} Z_n(\beta r) P_n^m(\cos(\theta)) \sin(m\varphi) + \hat{a}_\theta \frac{1}{\beta r} \frac{\partial}{\partial r} [r Z_n(\beta r)] \frac{\partial}{\partial \theta} P_n^m(\cos(\theta)) \sin(m\varphi) \\ &\quad + \hat{a}_\varphi \frac{m}{\sin(\theta)} \frac{1}{\beta r} [r Z_n(\beta r)] \frac{\partial}{\partial \theta} P_n^m(\cos(\theta)) \cos(m\varphi) \end{aligned} \quad (5)$$

$$\begin{aligned} \mathbf{N}_{emn} &= \hat{a}_r \frac{n(n+1)}{\beta r} Z_n(\beta r) P_n^m(\cos(\theta)) \cos(m\varphi) + \hat{a}_\theta \frac{1}{\beta r} \frac{\partial}{\partial r} [r Z_n(\beta r)] \frac{\partial}{\partial \theta} P_n^m(\cos(\theta)) \cos(m\varphi) \\ &\quad - \hat{a}_\varphi \frac{m}{\sin(\theta)} \frac{1}{\beta r} [r Z_n(\beta r)] \frac{\partial}{\partial \theta} P_n^m(\cos(\theta)) \sin(m\varphi) \end{aligned} \quad (6)$$

In these equations, Z_n indicates the spherical Bessel or Hankel functions correspond to the direction of propagating wave. Also P_n^m is Associate Legendre function. In proceeding we use substitution indicated by Eq. (7):

$$\hat{Z}_n(\beta r) = \beta r Z_n(\beta r) \quad (7)$$

According to Fig. 1 we can expand electromagnetic fields by two vectors \mathbf{M} and \mathbf{N} :

$$\mathbf{E}^i = \sum_{n=1}^{\infty} \alpha_n \left[\mathbf{M}_{dn}^{(1)}(\beta_3, \mathbf{r}, \theta, \varphi) + j \mathbf{N}_{dn}^{(1)}(\beta_3, \mathbf{r}, \theta, \varphi) \right] \quad (8)$$

$$\mathbf{H}^i = \frac{j}{\eta_3} \sum_{n=1}^{\infty} \alpha_n \left[\mathbf{N}_{dn}^{(1)}(\beta_3, \mathbf{r}, \theta, \varphi) + j \mathbf{M}_{dn}^{(1)}(\beta_3, \mathbf{r}, \theta, \varphi) \right] \quad (9)$$

\mathbf{E}^i and \mathbf{H}^i are incident plane wave electromagnetic fields. Also in these equations β is wave number, η is characteristic impedance and coefficient α_n defined as:

$$\alpha_n = (-j)^n \frac{2n+1}{n(n+1)} \quad (10)$$

Scattered and transmitted waves in each layer can be expanded as Eqs. (11) to (18):

$$\mathbf{E}^{s3} = \sum_{n=1}^{\infty} \left[A_n^{s3} \mathbf{M}_{dn}^{(4)}(\beta_3, \mathbf{r}, \theta, \varphi) + j B_n^{s3} \mathbf{N}_{dn}^{(4)}(\beta_3, \mathbf{r}, \theta, \varphi) \right] \quad (11)$$

$$\mathbf{H}^{s3} = \frac{j}{\eta_3} \sum_{n=1}^{\infty} \left[A_n^{s3} \mathbf{N}_{dn}^{(4)}(\beta_3, \mathbf{r}, \theta, \varphi) + j B_n^{s3} \mathbf{M}_{dn}^{(4)}(\beta_3, \mathbf{r}, \theta, \varphi) \right] \quad (12)$$

$$\mathbf{E}^{t2} = \sum_{n=1}^{\infty} \left[A_n^{t2} \mathbf{M}_{dn}^{(1)}(\beta_2, \mathbf{r}, \theta, \varphi) + j B_n^{t2} \mathbf{N}_{dn}^{(1)}(\beta_2, \mathbf{r}, \theta, \varphi) \right] \quad (13)$$

$$\mathbf{H}^{t2} = \frac{j}{\eta_2} \sum_{n=1}^{\infty} \left[A_n^{t2} \mathbf{N}_{dn}^{(1)}(\beta_2, \mathbf{r}, \theta, \varphi) + j B_n^{t2} \mathbf{M}_{dn}^{(1)}(\beta_2, \mathbf{r}, \theta, \varphi) \right] \quad (14)$$

$$\mathbf{E}^{s2} = \sum_{n=1}^{\infty} \left[A_n^{s2} \mathbf{M}_{dn}^{(4)}(\beta_2, \mathbf{r}, \theta, \varphi) + j B_n^{s2} \mathbf{N}_{dn}^{(4)}(\beta_2, \mathbf{r}, \theta, \varphi) \right] \quad (15)$$

$$\mathbf{H}^{s2} = \frac{j}{\eta_2} \sum_{n=1}^{\infty} \left[A_n^{s2} \mathbf{N}_{dn}^{(4)}(\beta_2, \mathbf{r}, \theta, \varphi) + j B_n^{s2} \mathbf{M}_{dn}^{(4)}(\beta_2, \mathbf{r}, \theta, \varphi) \right] \quad (16)$$

$$\mathbf{E}^{t1} = \sum_{n=1}^{\infty} \left[A_n^{t1} \mathbf{M}_{dn}^{(1)}(\beta_1, \mathbf{r}, \theta, \varphi) + j B_n^{t1} \mathbf{N}_{dn}^{(1)}(\beta_1, \mathbf{r}, \theta, \varphi) \right] \quad (17)$$

$$\mathbf{H}^{t1} = \frac{j}{\eta_1} \sum_{n=1}^{\infty} \left[A_n^{t1} \mathbf{N}_{dn}^{(1)}(\beta_1, \mathbf{r}, \theta, \varphi) + j B_n^{t1} \mathbf{M}_{dn}^{(1)}(\beta_1, \mathbf{r}, \theta, \varphi) \right] \quad (18)$$

where, in Eqs. (11) to (18), superscript (1) stands for spherical Bessel functions j_n and superscript (4) for spherical Hankel functions $h_n^{(2)}$, which we faced in \mathbf{M} and \mathbf{N} [2]. And also s and t superscripts in coefficients stand for scattered and transmitted waves in each layer.

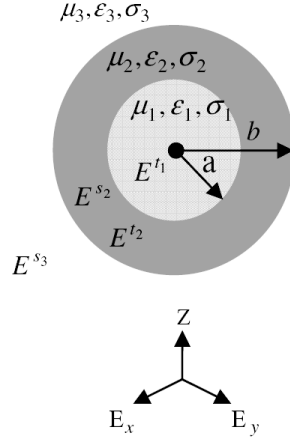


Figure 1: A plane wave incident to the two layer spherical dielectric resonator.

Let us assume that $\mu_1 = \mu_2 = \mu_3 = \mu_0$ and $\sigma_1 = \sigma_2 = \sigma_3 = 0$, by applying the boundary conditions we will have two different matrixes for TE and TM modes, separately.

$$\begin{bmatrix} -h_n^{(2)}(\beta_3 b) & h_n^{(2)}(\beta_2 b) & j_n(\beta_2 b) & 0 \\ -\hat{h}'_n^{(2)}(\beta_3 b) & \hat{h}'_n^{(2)}(\beta_2 b) & \hat{j}'_n(\beta_2 b) & 0 \\ 0 & h_n^{(2)}(\beta_2 a) & j_n(\beta_2 a) & -j_n(\beta_1 a) \\ 0 & \hat{h}'_n^{(2)}(\beta_2 a) & \hat{j}'_n(\beta_2 a) & -\hat{j}'_n(\beta_1 a) \end{bmatrix} \begin{bmatrix} A_n^{s3} \\ A_n^{s2} \\ A_n^{t2} \\ A_n^{t1} \end{bmatrix} = \begin{bmatrix} \alpha_n j_n(\beta_3 b) \\ \alpha_n \hat{j}'_n(\beta_3 b) \\ 0 \\ 0 \end{bmatrix} \quad (19)$$

$$\begin{bmatrix} -\hat{h}'_n^{(2)}(\beta_3 b) & \sqrt{\frac{\epsilon_3}{\epsilon_2}} \hat{h}'_n^{(2)}(\beta_2 b) & \sqrt{\frac{\epsilon_3}{\epsilon_2}} \hat{j}'_n(\beta_2 b) & 0 \\ -h_n^{(2)}(\beta_3 b) & \sqrt{\frac{\epsilon_2}{\epsilon_3}} h_n^{(2)}(\beta_2 b) & \sqrt{\frac{\epsilon_2}{\epsilon_3}} j_n(\beta_2 b) & 0 \\ 0 & \sqrt{\frac{\epsilon_1}{\epsilon_2}} \hat{h}'_n^{(2)}(\beta_2 a) & \sqrt{\frac{\epsilon_1}{\epsilon_2}} \hat{j}'_n(\beta_2 a) & -\hat{j}'_n(\beta_1 a) \\ 0 & \sqrt{\frac{\epsilon_2}{\epsilon_1}} h_n^{(2)}(\beta_2 a) & \sqrt{\frac{\epsilon_2}{\epsilon_1}} j_n(\beta_2 a) & -j_n(\beta_1 a) \end{bmatrix} \begin{bmatrix} B_n^{s3} \\ B_n^{s2} \\ B_n^{t2} \\ B_n^{t1} \end{bmatrix} = \begin{bmatrix} \alpha_n \hat{j}'_n(\beta_3 b) \\ \alpha_n j_n(\beta_3 b) \\ 0 \\ 0 \end{bmatrix} \quad (20)$$

The solution of these two complex equations will give us the resonant frequencies and quality factors of multilayer dielectric resonators.

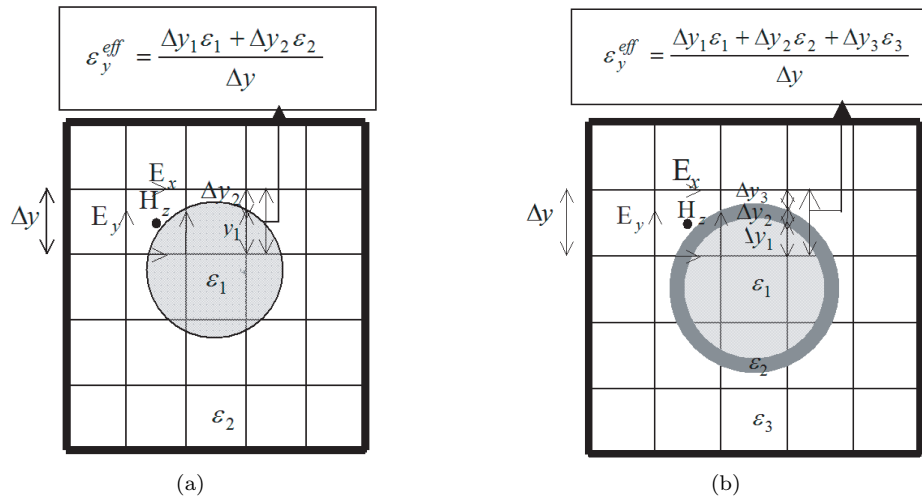


Figure 2: (a) Mesh truncation of a spherical DR and (b) Mesh truncation of a thin layer spherical DR.

3. CFDTD Method

The CFDTD can reduce the error introduced by staircasing in Cartesian coordinate. The effective dielectric permittivity of dielectric material in any piece of stairs can be found by following equations [1].

$$\epsilon_x^{eff} = \frac{\Delta x_1 \epsilon_1 + \Delta x_2 \epsilon_2}{\Delta x} \tag{21}$$

$$\epsilon_y^{eff} = \frac{\Delta y_1 \epsilon_1 + \Delta y_2 \epsilon_2}{\Delta y} \tag{22}$$

$$\epsilon_z^{eff} = \frac{\Delta z_1 \epsilon_1 + \Delta z_2 \epsilon_2}{\Delta z} \tag{23}$$

where, by applying these values in split Maxwell equations, the error of staircasing will be reduced.

In the case of thin layer surface, such as a spherical shell DR, Yee cells may contain three or more dissimilar dielectrics. In such cases, such as n different dielectric layers, we use average method.

$$\epsilon_x^{eff} = \frac{\Delta x_1 \epsilon_1 + \Delta x_2 \epsilon_2 + \Delta x_3 \epsilon_3 + \dots + \Delta x_n \epsilon_n}{\Delta x} \tag{24}$$

$$\epsilon_y^{eff} = \frac{\Delta y_1 \epsilon_1 + \Delta y_2 \epsilon_2 + \Delta y_3 \epsilon_3 + \dots + \Delta y_n \epsilon_n}{\Delta y} \tag{25}$$

$$\epsilon_z^{eff} = \frac{\Delta z_1 \epsilon_1 + \Delta z_2 \epsilon_2 + \Delta z_3 \epsilon_3 + \dots + \Delta z_n \epsilon_n}{\Delta z} \tag{26}$$

Table 1: Comparison of resonant frequencies found by CFDTD simulation and Ref. [4], for a cylindrical DR with $\epsilon_r = 38$, $a = 5.25$ mm and $h = 4.6$ mm.

Mode	Frequency (GHz)		Relative Error
	Ref. [4]	CFDTD	
TE _{01δ}	4.829	4.859	%0.621
HEM _{11δ}	6.333	6.299	%0.536
HEM _{12δ}	6.638	6.694	%0.843
TM _{01δ}	7.524	7.487	%0.491
HEM _{21δ}	7.752	7.702	%0.644

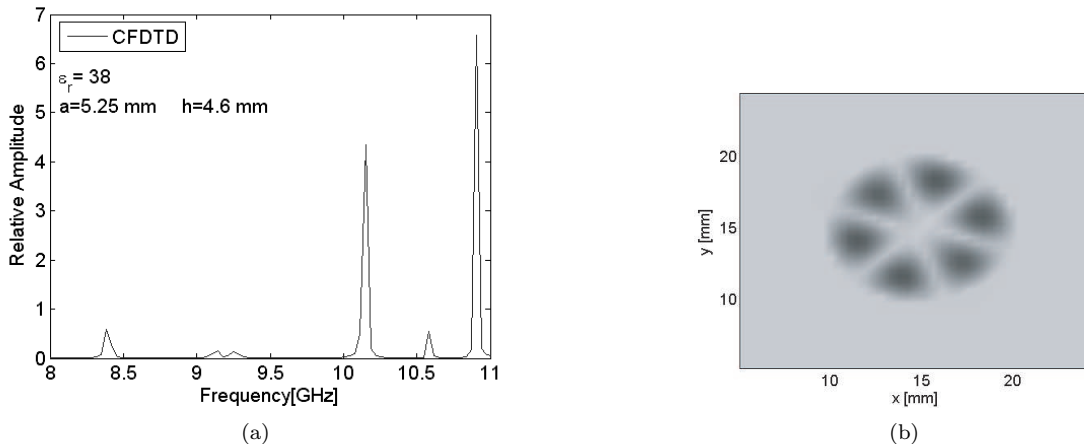


Figure 3: (a) Resonant frequency response of a cylindrical DR with $\epsilon_r = 38$, $a = 5.25$ mm and $h = 4.6$ mm found by CFDTD and (b) Plot of H field at $f = 10.1507$ GHz.

4. Numerical Results

In this section the results of CFDTD simulation for cylindrical and thin layer spherical DRs are shown. For verification, the results are compared with analytical (exact) method or with other reference data.

4.1. Cylindrical Dielectric Resonator

Let us use cylindrical DR with following electrical and geometrical parameters: $\varepsilon_r = 38$, radius $a = 5.25$ mm and height $h = 4.6$ mm. In table 1, resonant frequencies found by CFDTD simulation and Ref. [4] are compared. Also in Fig. 3, frequency response of the cylindrical DR and plot of H field, stimulated at $f=10.1507$ GHz, are shown.

4.2. Thin Layer Spherical Dielectric Resonator

A thin layer spherical DR with $\varepsilon_r = 90$, external radius $b = 2.54$ cm and internal radius $a = 0.99b$ is simulated with CFDTD method. We have compared our results with Mie method and it is fairly good. As it is shown in Fig. 4(b), Whispering Gallery Mode is stimulated in the thin layer spherical DR at $f = 35.3214$ GHz.

5. Conclusion

In this article, we have presented CFDTD simulation of dielectric resonators. A cylindrical DR has been simulated, and a good agreement with Ref. [4] is achieved. For the next simulation, a thin layer spherical dielectric resonator is considered and we faced with Whispering Gallery Modes which we have predicted by Mie method.

These simulations will show us that CFDTD method can give us very good results for simulating resonant frequencies of any shaped dielectric resonators.

Acknowledgment

The authors wish to thank Iran Telecommunications Research Center for encouragement and sponsoring this work.

REFERENCES

1. Dey, S. and R. Mittra, "A conformal finite difference time domain technique for modeling cylindrical dielectric resonators," *IEEE Transactions on Microwave Theory & Techniques*, Vol. 47, No. 9, 1737–1739, September 1999.
2. Stratton, J. A., *Electromagnetic Theory*, McGraw-Hill, New York, 1941.
3. Tobar, M. E., J. D. Hartnett, and J. Anstie, "Proposal for a michelson-morley experiment using whispering spherical mode resonators," *Physics Letters A*, Vol. 300/1, 33–39, 2000.
4. Kajfez, D. and P. Guillon, *Dielectric Resonators*, Artech House, Norwood, MA, 1986.
5. Taflove, A. and S. C. Hagness, *Computation Electrodynamics: The Finite-Difference Time-Domain Method*, Artech House, Norwood, MA, 2000.
6. Berenger, J. P., "Perfectly matched layer for absorption of electromagnetic waves," *Journal of Computational Physics*, Vol. 114, No. 2, 185–200, 1994.

A Novel Transmission Line Model for Analyzing Bowtie Patch Antennas

K. Moussakhani and A. Ghorbani
Amirkabir University of Technology, Iran

Abstract—A novel transmission line model is represented to model bowtie patch antennas. The purposed model uses two slots for modeling the radiation from patch sides. Each radiation slot is presented by parallel equivalent admittance. Also in this model mutual coupling and the effect of slots length limitation as well as the influence of the side slots on the radiation conductance are taken into account implicitly. Admittance and controlled source equations that used for rectangular patch antenna are modified.

1. Introduction

These days microstrip antennas are popular and getting more and more attention due to their excellent advantages. Depending upon the applications, microstrip antennas having different geometrical shapes are used. In other hand now days researchers are interested in the design and development of compact microstrip radiating elements. It can be argued that Bowtie microstrip antenna is one of such compact microstrip antennas [2]. The Bowtie antenna dose not has a regular geometric shape and hence most of the analytical techniques such cavity model can not be used for antenna’s parameter calculation directly. However, popular numerical techniques like method of moment (MOM), finite element method, finite-difference time -domain (FDTD) method, etc., could be used for analysis of such antennas but they are computationally expensive.

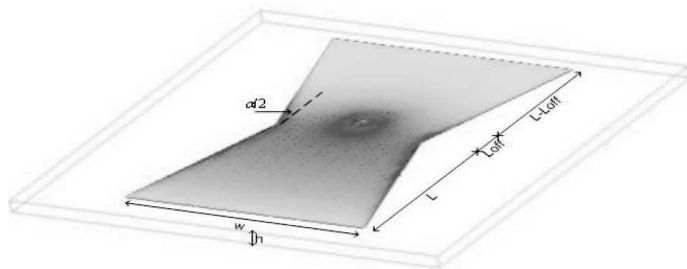


Figure 1: Antenna structure.

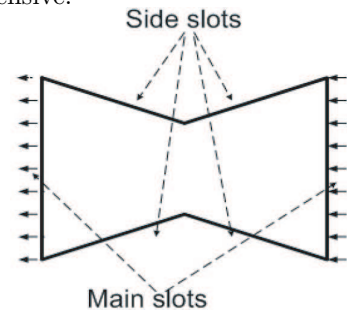


Figure 2:

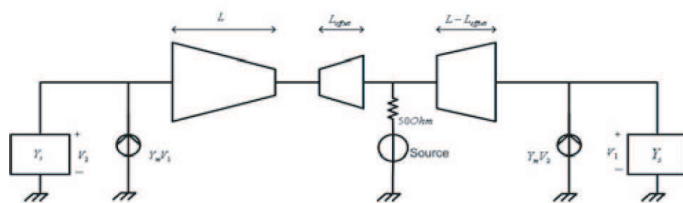


Figure 3: Antenna structure.

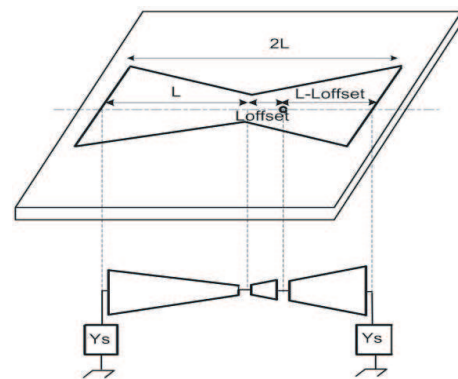


Figure 4:

The transmission line method (TLM) is known to be reasonably accurate and have good efficiency especially in numerical calculation as well as it can be applied for modeling of antennas arrays. Therefore in this paper a novel transmission line model is presented for analysis of bowtie patch antenna of finite length, placed on a dielectric substrate as shown in Fig. 1. Also Fig. 2 shows the radiating slots which form a useful model for calculating the radiation field of the antenna. These so-called equivalent slots consist of two main slots with a uniform distribution and four side slots with sinusoidal distribution.

In order to model regular microstrip antenna with the existing transmission-line models, shape of the antenna represented by a line section terminated at both ends by radiation admittance. Also an improved TLM model for rectangular microstrip antenna has been introduced by Pues and Van de Cappelle which used voltage dependent current generators for modeling mutual coupling [1].

Our model in this paper is similar to Pues model [1] in addition we have used taper transmission line instead normal microstrip line for modeling bowtie shaped patch as shown in Fig. 3. More over as can be seen in Fig. 3 the offset of feed location has been considered by dividing the taper line into two sections.

2. Determination of Model Parameters

Figure 4 model contains of following unknowns:

1. The line parameters (Y_c).
2. The self admittance of slots (Y_s).
3. The mutual admittance (Y_m).

Where each term can be define and calculated as follow:

2.1. Line Parameters

Characteristic impedance could be calculated by:

$$Z_c = \frac{\eta_0}{\sqrt{\epsilon_e}} \frac{h}{W_e}$$

$$W_e = \frac{W + W_c}{2}$$

where

2.2. Self Admittance

In order to determine $Y_s (= G_s + jB_s)$, previous works for rectangular microstrip antennas have been examined for improving the accuracy and efficiency of our model. In this respect Pues formula [1] is used for determining the self conductance G_s .

$$G_s = \frac{1}{\pi\eta} \left\{ (w \operatorname{Si}(w) + \frac{\sin w}{w} + \cos w - 2) \left(1 - \frac{s^2}{24}\right) + \frac{s^2}{12} \left(\frac{1}{3} + \frac{\cos w}{w^2} - \frac{\sin w}{w^3}\right) \right\}$$

And for susceptance we used Pues formula [1] as given by:

$$B_s = Y_s \tan(\beta\Delta l)$$

Where the open end effect can be calculated as:

$$\frac{\Delta l}{h} = 0.412 \frac{\epsilon_e + 0.300 W_e/h + 0.262}{\epsilon_e - 0.258 W_e/h + 0.813}$$

2.3. Mutual Admittance

Accurate closed-form expressions have been derived for both the real and imaginary parts of mutual admittance $Y_m = G_m + jB_m$ for rectangular microstrip antenna by Pues [1]. In order to determine the Mutual admittance we used the Pues formula as follow:

$$G_m = K_g F_g G_s$$

where

$$K_g \approx 1$$

$$F_g \approx J_0(l) + \frac{s^2}{24 - s^2} J_2(l)$$

and

$$B_m = K_b F_b B_s$$

where

$$F_b = \frac{b_m}{b_s} \approx \frac{\pi}{2} \frac{Y_0(l) + \frac{s^2}{24 - s^2} Y_2(l)}{\ln\left(\frac{s}{2}\right) + C_e - \frac{3}{2} + \frac{s^2/12}{24 - s^2}}$$

$$k_b = 1 - \exp(-0.21w)$$

3. Results

For different flare angle of bowtie patch antenna we calculated the antenna parameters as stated above then we compared results of return loss obtained from the purposed model with results obtained by Advanced Design System where uses MoM.

As seen in Fig. 5 good agreement have been achieved for different flare angles. Also the error between the two methods increase by increasing flare angle from 3% for $\alpha = 10^\circ$ to 5% for $\alpha = 30^\circ$. For small flare angle the results of purposed model have good agreements with full wave results, but as the flare angle increased the results are not in good agreement because of radiations from side slots. As this radiations are more effective in higher flare angle so for large flare angle this model are not valid anymore.

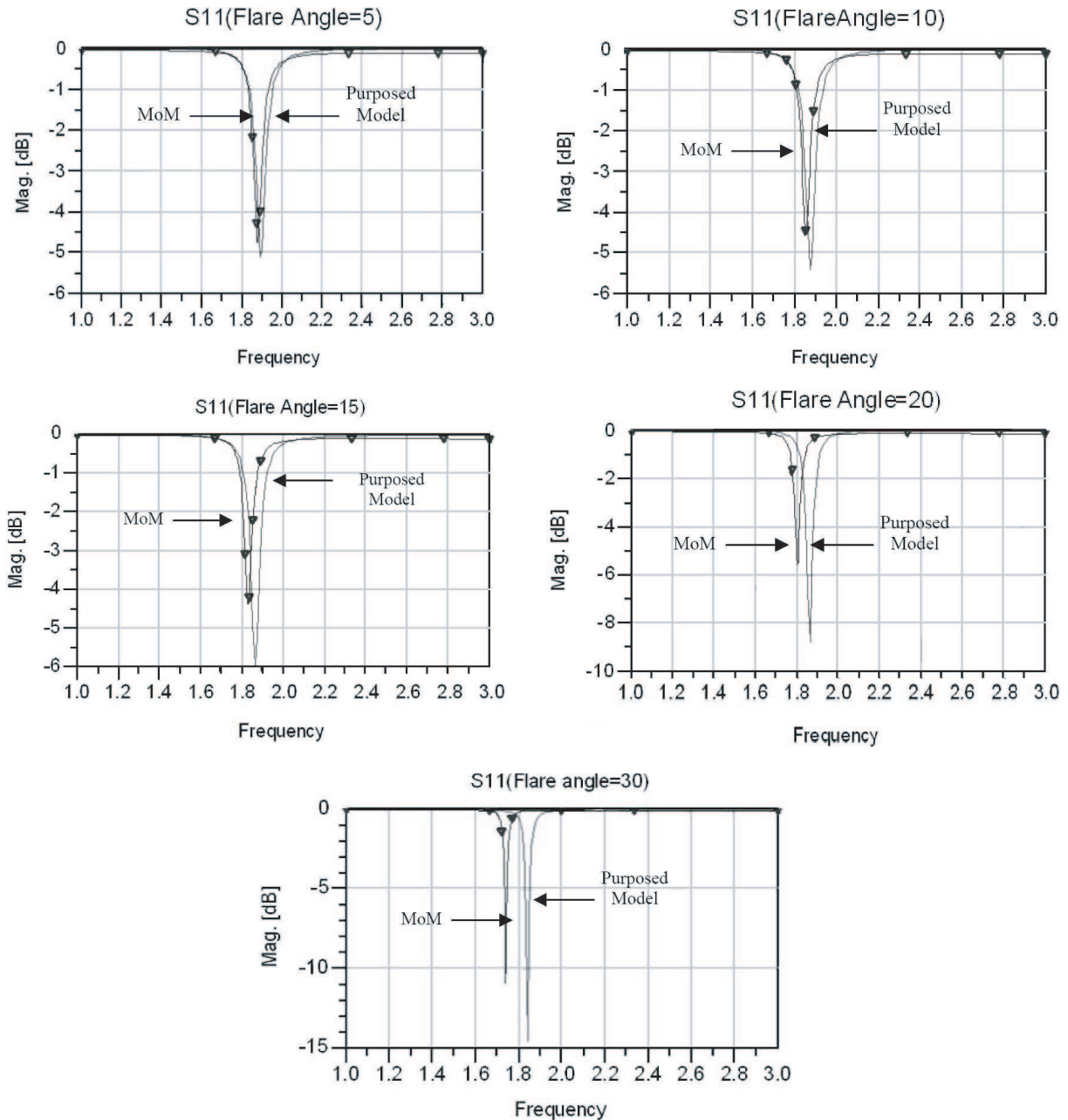


Figure 5: Return Loss for different flare angles.
 $\epsilon = 4.4$, $h = 1.6$ mm, $L = 18.75$ mm, $W = 25.2$ mm

4. Conclusion

A novel transmission line model is represented for modeling the bowtie patch antennas. Admittance and controlled source equations used in the passed for rectangular patch antennas have been modified in this model for bowtie patch antenna. This model is just valid for a moderate range of flare angles and results are reasonably

accurate in that region and therefore this approach can be used as TLM for bowtie patch antenna for evaluating antenna parameters.

Acknowledgement

This work is supported by Iran Telecommunication research center (ITRC).

REFERENCES

1. Pues, H. and A. van de Cappelle, "Accurate Transsmission-line model for the reactangular microstrip antenna," *Proc. IEE*, Vol. 131, pt. H., No. 6, Dec. 1984.
2. George, J., C. K. Aanandan, P. Mohanan, and K. G. Nair, "Analysis of a new compact microstrip antenna," *IEEE Transactions on Antennas and Propagation*, Vol. 46, Issue 11, 1712–1717, Nov. 1998.
3. Munson, R., "Conformal microstrip antennas and microstrip phased arrays," *IEEE Transactions on Antennas and Propagation [legacy, pre - 1988]*, Vol. 22, Issue 1, 74–78, Jan. 1974.
4. Derneryd, A., "A theoretical investigation of the rectangular microstrip antenna element," *IEEE Transactions on Antennas and Propagation [legacy, pre - 1988]*, Vol. 26, Issue 4, 532–535, Jul. 1978.
5. George, J., M. Deepukumar, C. K. Aanandan, P. Mohanan, and K. G. Nair, "New compact microstrip antenna," *Electronics Letters*, Vol. 32, Issue 6, 508–509, 14 March 1996.